REVIEW ARTICLE

Check for updates

Photothermal catalytic C1 conversion on supported catalysts

Hui Liu,[a] Liangliang Han, [ID][a] Xiaoguang Duan, [ID][b] Hongqi Sun, [ID][c] Shaobin Wang [ID][b] and Jinqiang Zhang [ID] *[b]

Photothermal catalysis has emerged as a robust approach for converting C1 feedstocks into valuable chemicals, providing a clean and sustainable alternative that reduces the carbon footprint and enables energy-efficient green synthesis. Supported metal materials are promising candidates for scaling up photothermal catalysis, as their photothermal properties can be precisely tailored to optimize energy conversion efficiency and product distribution for specific processes. In this review, we provide an in-depth examination of the application of supported catalysts in photothermal catalytic C1 chemistry, which begins with an introduction of the mechanism of photothermal catalysis and elucidation of the fundamental principles behind this process. An overview of the design strategies for supported catalysts follows, encompassing various techniques for tailoring their properties to meet specific catalytic requirements. Advancements made in utilizing supported catalysts for photothermal catalytic reactions in C1 chemistry are then highlighted. Finally, challenges in the fledgling field are summarized and valuable insights into the future development directions and focuses are provided. This comprehensive review is anticipated to offer a deeper understanding of the design, performance, and potential applications of supported catalysts in photothermal catalysis for C1 chemistry, transforming conventional chemical processes into 'green'.

1. Introduction

The current chemical industry faces a critical challenge as it heavily relies on fossil fuels to produce commodity chemicals and energy sources. However, this dependence on non-renewable resources is not sustainable due to limited reserves and the release of harmful greenhouse gases into the atmosphere. To address these issues, the industry must find alternative ways to manufacture chemicals without solely relying on

*[a] College of Chemistry and Chemical Engineering, Yantai University, Yantai 264005, China*

[b] School of Chemical Engineering, The University of Adelaide, North Terrace, Adelaide, SA 5005, Australia. E-mail: jinqiang.zhang@adelaide.edu.au

[c] School of Molecular Sciences, The University of Western Australia, 35 Stirling Highway, Perth, WA 6009, Australia

Dr Hui Liu received her PhD in chemical engineering and technology from China University of Petroleum (East China). She is now a lecturer at the College of Chemistry & Chemical Engineering, Yantai University, China. Her research interests primarily focus on the synthesis and application of nanomaterials for catalysis, encompassing electrocatalysis and photoelectrochemical catalysis for energy conversion and utilization.

Hui Liu

Dr Jinqiang Zhang received his PhD from Edith Cowan University, Australia. He is now a research fellow at the School of Chemical Engineering, The University of Adelaide, Australia. His research interests focus on photo-mediated catalysis, including photocatalysis, photoelectrochemical catalysis and photothermal catalysis, for energy preparation and fossil fuel upgrading.

Jinqiang Zhang

fossil fuels. C1 chemistry offers a revolutionary approach by converting simple C1 molecules such as CO, CO_2, CH_4, and CH_3OH into advanced fuels and chemicals.[1,2] This process can also produce high-quality hydrogen and premium specialty chemicals from synthesis gas or methanol. By harnessing the power of C1 chemistry, a sustainable supply model can be created, reducing dependence on traditional fossil fuels. Currently, the industry typically requires harsh reaction conditions, including high temperature and pressure, to achieve significant conversion of C1 molecules. For example, methane, the most stable alkane molecule,[3,4] necessitates high temperatures (600–1100 °C) for effective activation and conversion.[5] However, these conditions result in high energy consumption, environmental issues, and catalyst deactivation. Therefore, it is crucial to seek mild reaction conditions to reduce energy input, lower temperature requirements, and achieve robust C1 transformation at atmospheric pressure.

In recent years, photothermal catalysis has emerged as a promising approach that utilizes solar energy to replace conventional heating means to trigger catalytic reactions.[6,7] This innovative method offers several advantages over traditional thermal catalysis, notably the ability to drive reactions at moderate temperature and pressure using solar energy.[8] This reduces the need for costly equipment and infrastructure while promoting sustainability by minimizing reliance on non-renewable resources and reducing harmful emissions. Despite significant advances in solar technology, there is still room for improvement in enhancing the efficiency of solar energy conversion. To address this challenge, researchers are actively exploring new materials and innovative designs to enhance optical properties and minimize heat losses during catalysis.

Supported metal catalysts with dispersed nanoparticles have garnered significant interest, as their photothermal properties and catalytic capabilities can be precisely tuned by tailoring the geometrical configuration of the metal and support, and their interactions.[9] For example, reducing the size of metal nanoparticles can enhance solar-to-thermal conversion efficiency by increasing the number of accessible active sites. However, small metal species often suffer from poor stability and recyclability due to severe aggregation during catalysis, particularly under harsh conditions.[10] Loading catalysts onto appropriate supports has emerged as an attractive strategy to reduce costs and maximize atom utilization. However, the understanding of the structure–activity relationship and reaction mechanisms in composite systems is still in its early stages.[11] Supported catalysts are more intricate than their single-phase counterparts as they involve catalytically active phases and supports that work in tandem. Understanding their electronic/chemical properties, strong metal–support interactions (SMSIs), and working principles is essential to comprehend these intricate catalysts and their potential applications.

In this comprehensive review, we delve into the fascinating world of photothermal catalysis and explore its intricate mechanisms. Our aim is to provide a detailed understanding of the photochemical and photothermal effects that underpin this cutting-edge technology, as well as their synergistic coupling.
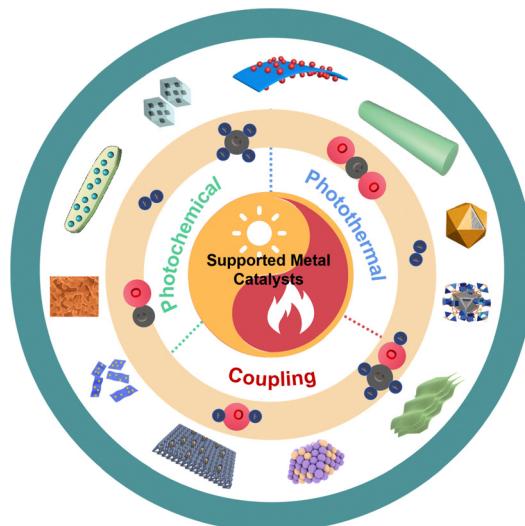

Fig. 1 Summary of photothermal catalytic C1 conversion using supported metal catalysts in this work.

Then, we explore the two important components (active and support components) in supported metal catalysts and conduct an in-depth exploration of their design strategies. Additionally, we comprehensively examine the recent advancements in supported metal catalysts for photothermal catalytic C1 chemistry. This includes the conversion of CO (such as Fischer–Tropsch synthesis and water-gas-shift reaction), CO_2 (reverse water-gas-shift reaction, methanation, methanol and higher hydrocarbon production), and methane (oxidation, non-oxidative coupling, steam and dry reforming) (Fig. 1). Finally, we provide a concise summary of the current research challenges and prospects within this field. This review contributes fundamental knowledge to the emerging field and holds the potential to revolutionize conventional chemical processes in a green and sustainable manner.

2. Mechanism of photothermal catalytic C1 chemistry

Photothermal catalysis represents an emerging technology that harnesses the synergy between photo and thermal energy to enhance catalytic activity and selectivity, enabling alternative reaction pathways. In the realm of C1 chemistry, the conversion of C1 molecules necessitates the cleavage of C–O/C=O/C–H bonds, demanding a significant driving force. Photothermal catalysis can be categorized into three modes, depending on the primary driving force: photo-assisted thermocatalysis, thermal-assisted photocatalysis, and photothermal synergistic catalysis.[6,12] In order to facilitate the design and development of more resilient catalysts, we, in this section, present a comprehensive analysis of the mechanisms governing photothermal catalytic C1 chemistry, elucidating its intricate and multifaceted steps.

2.1 Photochemical effect

Photochemical processes involve the excitation of semiconductors, leading to the generation of charge carriers (photogenerated

electrons and holes) that migrate to the semiconductor surface and participate in chemical reactions with adsorbed molecules.[13] Since the groundbreaking work of Fujijima and Honda in 1972, significant advancements have been made in the field of photocatalysis.[14] However, most photocatalytic processes still suffer from low efficiency, primarily due to rapid carrier recombination and limited solar spectrum absorption and utilization by conventional wide-band gap semiconductors. This limitation has driven the rise of photothermal catalysis as a technology to improve photocatalytic activity.[15]

In addition, noble metal nanoparticles, such as Au, Ag, and Cu, can harness the wide solar spectrum (including visible and infrared light regions) through the strong localized surface plasmon resonance (LSPR) effect.[16] These nanoparticles then undergo energy dissipation through three pathways: First, a significant portion of energy is absorbed within the metal nanoparticles, generating energetic hot charge carriers, primarily hot electrons, through non-radiative decay (Landau damping process).[17] These energetic hot charge carriers further induce chemical reactions. Second, a small fraction of the non-radiative decay energy transfers to the metal lattice phonons, resulting in localized heating known as plasmonic-induced thermal effects (Section 2.2). The remaining minor amount of energy is re-emitted as photons through radiation decay, augmenting the optical near-field. It is worth noting that the first two pathways play crucial roles in photothermal catalysis.

2.2 Photothermal effect

The photothermal effect is a phenomenon frequently observed in photo-driven thermal catalysis. In this process, the catalyst utilizes incident light to generate thermal energy (heat) upon irradiation, thereby elevating the surface temperature to facilitate catalytic reactions. Photothermal catalysis stands out among other solar energy harnessing technologies due to its exceptional efficiency in energy conversion. The photothermal effect in the catalyst arises from various mechanisms, including non-radiative relaxation in semiconductors, plasmonic localized heating, and thermal vibration of molecules.[18] Fig. 2 demonstrates that different photothermal materials can convert light into heat through one or more pathways of photothermal conversion.

When light illuminates a semiconductor, photons with energy equal to or greater than the bandgap can excite the semiconductor, resulting in the generation of electron–hole pairs. These partial electrons and holes have the ability to migrate to the surface of a catalyst and participate in redox reactions. A significant portion of the electron–hole pairs releases energy through both radiative and non-radiative dissipation mechanisms. The non-radiative dissipation process induces phonons, which leads to heat energy generation through lattice vibration. This phenomenon, known as the photothermal effect in semiconductors, relies on the generation of charge carriers through photoexcitation. Similarly, the LSPR effect of plasmonic nanomaterials generates charge carriers, including high-energy hot electrons, that drive photochemical reactions. The non-radiative relaxation in plasmonic materials also contributes to local heating through electron–phonon scattering, thereby enhancing the activity of photothermal catalysis.

In addition to semiconductors and plasmas, photothermal effects can be observed in other materials with strong light absorption capacities, such as carbon-based materials (carbon nanotubes, graphene, amorphous carbon, etc.), metal–organic frameworks (MOFs), and mexenes.[19–30] When these materials are excited by light, electrons undergo transitions from the highest occupied molecular orbital (HOMO) of the ground state to the lowest unoccupied molecular orbital (LUMO) of a higher energy state. Subsequently, through electron-vibrational relaxation processes, heat energy is generated. This photothermal conversion primarily occurs through thermal vibration in molecules.

2.3 Coupling of photochemical and photothermal effects

The photothermal catalytic process involves a complex interplay between the photochemical effect and photothermal effect,
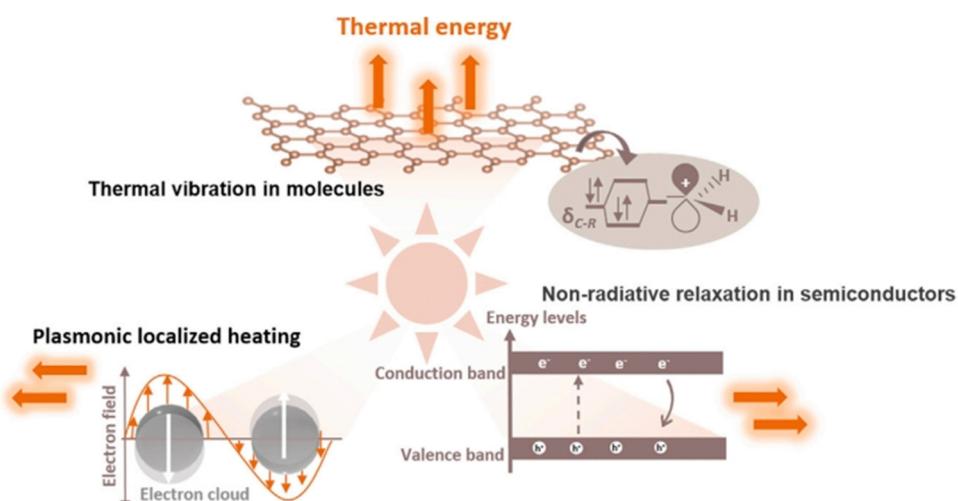

Fig. 2 Different mechanisms of photo-to-thermal process in various materials.[18]

as these two phenomena are intricately connected and jointly determine the overall outcome. In the photochemical process, carriers excited by semiconductor photocatalysts or plasmonic materials act as driving forces for chemical reactions. The hot carriers generated through light irradiation actively participate in catalytic reactions, constituting the photochemical effect. On the other hand, the thermocatalytic process in photothermal catalysis relies on the non-radiative relaxation of semiconductors, plasmonic localized heating, and thermal vibration in molecules. These factors play pivotal roles in converting light into heat. The photothermal effect enables efficient dissipation of absorbed photon energy as heat under light irradiation, facilitating carrier transfer and enhancing catalytic activity. Furthermore, photothermal catalysis has the advantage of reducing or eliminating the need for additional heat input and energy consumption. The process concentrates most of the heat on the catalyst's surface, leading to high energy utilization rates. In certain cases, photothermal catalysis effectively prevents catalyst deactivation and enhances the selectivity of desired products. Therefore, the reaction mechanism of heterogeneous photothermal catalysis typically involves the coupling of both photochemical and photothermal effects, representing the interplay between these phenomena.[31]

3. Design of supported metallic photothermal catalysts

Supported catalysts are materials where the active component is uniformly dispersed and supported on a carefully chosen substrate. Typically, supported catalysts consist of two main elements: the active component and the support component. In certain cases, the support component can also exhibit catalytic activity. These two components work together synergistically, resulting in a combined effect that exceeds the sum of their individual contributions. An effective photothermal catalyst should possess specific capabilities, including (1) strong light absorption, (2) high efficiency in photothermal conversion and heat retention, and (3) excellent catalytic activity, product selectivity, and stability. Therefore, the design and modification of catalysts primarily focus on enhancing light absorption across the solar spectrum, promoting efficient heat generation and transfer, and improving catalytic kinetics. In the following section, we will discuss the design strategies for the active and support components in supported catalysts separately, considering their respective roles and functionalities.

3.1 Design of active components

Metals possess exceptional properties which make them indispensable in various industries. Their efficient conductivity of electricity and heat makes them ideal for applications such as electrical wiring, power generation systems, and sustainable heating solutions. Additionally, metals exhibit efficient solar energy absorption and conversion capabilities, making them increasingly popular as a sustainable heat source for homes and buildings. By harnessing the power of the sun through

metal-based technologies like solar panels or thermal collectors, we can reduce our reliance on non-renewable energy sources such as fossil fuels and significantly decrease our carbon footprint. Therefore, metals are versatile and valuable resources that play an essential role in the functioning of modern society. Their unique combination of conductivity and solar absorption capabilities makes them vital components in numerous critical applications today while offering promising solutions for future renewable energy needs.

The LSPR effect plays a crucial role in determining the optical properties of metal nanomaterials. When nanometals are exposed to light with suitable energy, they induce the generation of energetic hot carriers and localized thermal energy, triggering chemical reactions. Previous research studies have demonstrated the remarkable responsiveness of plasmonic metal nanostructures to visible and near-infrared light.[32,33] The LSPR effect involves three pathways (Section 2.1) which provide the necessary energy for catalytic reactions to occur on the surface of metal nanostructures. Enhancing the LSPR effect of plasmonic nanomaterials is an effective strategy for broadening the optical absorption spectrum, improving photothermal conversion rates, and enhancing catalytic performance.

In photothermal catalysis, metals in photothermal catalysts primarily include precious metals (Au,[34] Ag,[35] Ru,[36] Rh,[37,38] Pd,[39,40] Ir, and Pt[41]) and non-precious metals (Fe,[42] Co,[43] Ni,[44] Cu,[45] Al,[46,47] and Nb[28]). By precisely controlling their sizes, shapes, and compositions, their photothermal catalytic performance can be tailored. In a recent study, Yang et al. achieved continuous size regulation of monodisperse Pd nanoparticles ranging from 2.8 to 8.1 nm (Fig. 3a). Through precise size control and manipulation of the surface electronic structure, the 6.3 nm Pd nanoparticles exhibited the highest catalytic activity in the photothermal catalytic hydrogenation of CO_2 to CO.[39] These findings illustrate that the catalytic activity of size-regulated nanoparticles is primarily influenced by the quantum size effect, metal–support interaction, and photothermal effect.

Single-atom catalysts (SACs) have emerged as promising candidates in catalysis due to their exceptional atomic utilization and unique electronic structures. Researchers have shown a growing interest in exploring the potential applications of SACs. In a study conducted by Guo et al., they constructed Pd_1/TiO_2 SACs through the selective encapsulation of co-existing Pd nanoclusters/nanoparticles based on different conditions of SMSI occurrence (Fig. 3b).[40] By utilizing detailed characterization techniques and density functional theory (DFT) calculations, the team gained valuable insights into the behavior of these SACs. The results were intriguing, as photo-induced electrons transferred from TiO_2 to adjacent Pd atoms, facilitating acetylene activation and highlighting the potential of these SACs in various catalytic reactions.

However, the excessive surface free energy of single-atom metals makes them susceptible to agglomeration at high temperatures, resulting in a significant reduction in the exposed metal surface area, a phenomenon known as sintering. This process adversely affects catalytic reactivity and, in some cases, can render the catalyst inactive. Metal sintering occurs
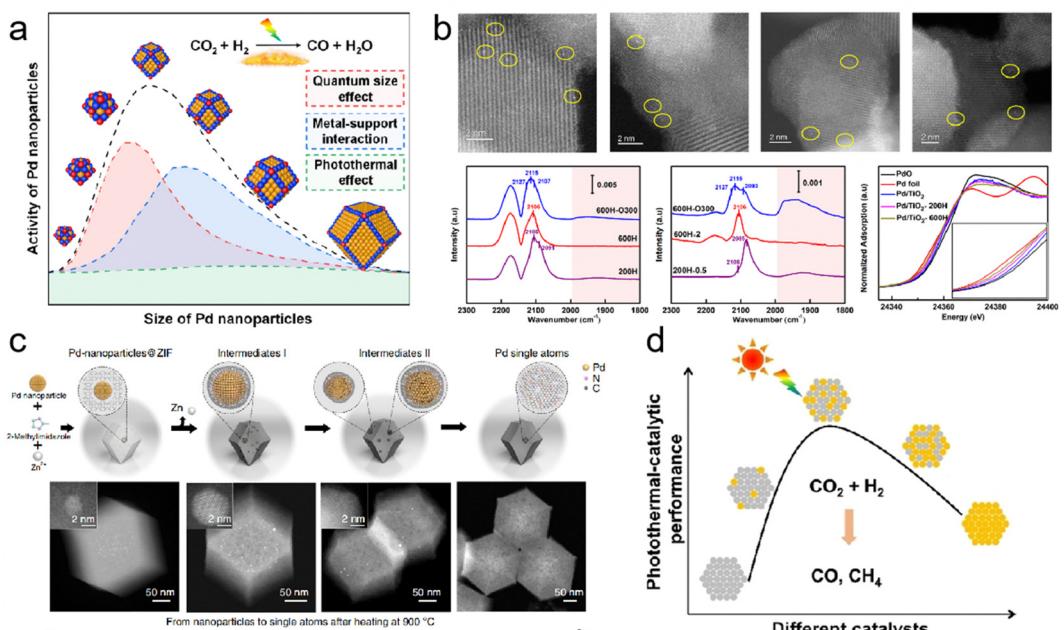
Fig. 3 (a) Monodispersed Pd nanoparticles with a narrow size distribution supported on TiO_2.[39] (b) Structural characterization of Pd/TiO_2 serial catalysts.[40] (c) Scheme of the transformation of nanoparticles to single atoms and structural characterization of Pd single atoms.[50] (d) The influence of the composition of bimetallic nanocrystals on photothermal catalytic performance.[51]

through two main pathways: migration between individual metal atomic nanoparticles or the coalescence of adjacent metal nanoparticles. It is worth noting that these pathways are not mutually exclusive and often occur simultaneously, particularly at elevated temperatures. To address this issue, researchers have explored strategies such as the introduction of SMSI or ligands to thermodynamically stabilize metal atoms. These approaches effectively reduce surface energy and limit the migration tendency of individual atoms. However, the use of certain ligands may have toxic effects, leading to deactivation of the catalyst. Alternatively, preventing collisions and coalescence kinetically can be achieved by confining metal nanoparticles within microporous solids such as zeolites and metal–organic frameworks.[48,49] A groundbreaking study by Wei *et al.* achieved a significant breakthrough in the field of nanotechnology.[50] The researchers successfully reversed the sintering process of nanoparticles by utilizing nitrogen-doped carbon (CN) as an anchoring substrate to capture migrating metal atoms at high temperatures (Fig. 3c). They employed ZIF-8 as the framework and transformed noble metal nanoparticles into highly active single atoms, including Pd, Pt, and Au. The resulting thermally stable particles exhibited exceptional catalytic activity. During the process of recording films with *in situ* environmental transmission electron microscopy (ETEM), an intriguing observation was made. Despite exposure to high temperatures, sintering occurred, causing smaller particles to fuse and form larger ones. However, as the Pd nanoparticle collided with the substrate, it gradually shrank and transformed into a single atom. The resulting thermally stable Pd single atoms exhibited superior catalytic activity and selectivity for acetylene semi-hydrogenation compared to Pd nanoparticles. This study presents a user-friendly top–down

approach for obtaining single-atom catalysts from nanoparticles and even reactivating sintered industrial precious metal nanocatalysts by dispersing them into individual atomic sites. These findings provide valuable insights for the development of high-performance, heat-stable catalysts.

In addition to the aforementioned strategies, the preparation of dispersed supported bimetallic nanocrystalline catalysts represents another feasible solution to enhance the performance of single-component metal catalysts. Chen *et al.* reported on the photothermal hydrogenation of CO_2 using Al_2O_3-supported CoFe alloy catalysts.[46] Their research demonstrated the effectiveness of these catalysts in the conversion process. Similarly, Zhu *et al.* developed a monodispersed Pd-Ni nanoalloys/SiO_2 catalyst, where the inclusion of Ni improved the optical absorption and photothermal conversion properties, while the presence of Pd enhanced the selectivity of the catalyst in converting CO_2 to CO (Fig. 3d).[51] These findings highlight the potential of dispersed supported bimetallic nanocrystalline catalysts in enhancing the performance and efficiency of catalytic processes.

However, the synthesis of these metal materials presents several challenges that need to be considered. Factors such as the wide range of metal materials available, the need for controllable morphology, environmental impact, high cost, and complex preparation processes should not be overlooked. Additionally, metal nanoparticles can undergo structural distortion when exposed to acids, bases, or salts, and they are susceptible to agglomeration under harsh conditions or contamination by trace impurities. Therefore, the careful selection of a suitable support material becomes crucial in ensuring the stability and functionality of the catalyst.

3.2 Design of support components

The support components of a catalyst play a crucial role in determining its overall performance, serving three primary functions that contribute to its efficiency. First, the support component provides an effective surface area and pore structure, which enhances catalytic activity by increasing the available surface area for reactions to occur. It also helps prevent the sintering or aggregation of the active component, which can lead to catalyst deactivation over time. Additionally, the support component increases the mechanical strength of the catalyst, making it more durable and resistant to wear and tear. Second, support components can provide additional active centers, particularly in bifunctional catalysts where multiple reactions occur simultaneously. These additional active centers contribute to improved reaction rates and selectivity. They can promote specific reaction pathways or provide sites for intermediate species adsorption, thereby enhancing the overall catalytic performance. Finally, the interaction between the support and active component is crucial in determining the catalytic activity and selectivity. The nature of this interaction depends on factors such as chemical composition, morphology, and size distribution, all of which influence the enhancement or inhibition of catalytic performance. Optimal support materials should exhibit strong interaction with the active component, facilitating charge transfer, promoting adsorption–desorption processes, and optimizing reactant accessibility.

Currently, inorganic semiconductors serve as the primary foundation for active metal components, providing a robust support system for photothermal catalysts. However, there are several other types of support materials commonly used in addition to semiconductors. These alternative supports include materials such as carbon, MXenes, and metal–organic frameworks (MOFs), each offering unique properties and advantages for specific photothermal applications.

3.2.1 Inorganic semiconductor. Inorganic semiconductors have become essential in conventional photocatalysis due to their numerous advantages. These materials are highly desirable for their ease of preparation, cost-effectiveness, low toxicity, and tunable band gap properties. However, the wide band gaps of most semiconductors limit their ability to absorb visible and infrared (IR) light, which constitutes most of the solar spectrum. This limitation hampers the full spectrum utilization of solar energy. Moreover, the efficiency of photocatalytic processes is often low due to the rapid recombination of photogenerated carriers caused by the wide band gaps of conventional semiconductors. Therefore, semiconductor design should focus on reducing the band gap and enhancing light absorption across the broad spectrum to promote photothermal catalytic performance through photochemical or photothermal effects.

To address these challenges, specific design strategies have been employed in the investigation of inorganic semiconductors. One prevalent method involves doping and/or introducing defects or vacancies to broaden the light absorption range and accelerate the separation of photogenerated carriers.[52,53] For example, treating molybdenum trioxide (m-WO_3) with pure hydrogen generates oxygen-deficient WO_3 (m-WO_{3-x}) catalysts,

exhibiting broader absorption from UV to near-infrared (NIR) light regions and narrower band gaps.[54] This transformation is attributed to the formation of oxygen vacancy-induced defect states in m-WO_{3-x}, which not only enhances catalytic activity but also expands the potential for photothermal conversion. Similarly, the introduction of defects into Bi_2O_{3-x} induces the LSPR effect in the near-infrared wavelength range, enhancing CO_2 molecule adsorption and enabling efficient photocatalysis of CO_2-to-CO even under low-intensity near-IR light irradiation.[55] Careful engineering of these imperfections allows customization of electronic and optical properties to meet specific requirements.

Another effective strategy for enhancing photothermal catalytic performance is coupling two types of inorganic semiconductors with different photocatalytic and thermal catalytic properties. Constructing heterojunctions with atomic arrangement and lattice mismatches can lead to remarkable light-to-hot carriers and light-to-thermal efficiency. S-scheme heterojunctions, in particular, have shown excellent photo-mediated conversion abilities (Fig. 4).[56–60] For example, Wang et al. synthesized a core–shell $Cu_{2-x}S@ZnIn_2S_4$ S-scheme heterojunction through a simple hydrothermal reaction, which broadened the absorption range of photocatalytic response, increased infrared light absorption, exhibited excellent photothermal effects, and promoted the photocatalytic reaction.[61,62] However, developing novel, facile, and clean approaches to produce engineered heterojunction materials with specific composites, sizes, and shapes remains a challenging task.

3.2.2 Carbonaceous materials. Carbonaceous materials are highly valued as catalyst supports due to their unique properties, such as tunability, chemical inertness, cost-effectiveness, and abundant availability. Notably, carbon exhibits exceptional photothermal characteristics, enabling it to absorb the entire spectrum of light. However, it is important to recognize that carbon-based materials have relatively high emissivity (approximately 0.85) due to their high surface reflectance.[63] This necessitates addressing surface reflection to achieve optimal efficiency in solar energy conversion when using carbon nanomaterials as catalyst supports. One effective approach is to enhance the structure of carbon materials by incorporating nanostructures. This enhances their ability to internally refract and scatter light, reducing heat loss from the material's surface and enhancing overall light absorption.

Ren et al. developed a hierarchical graphene foam as a solar absorber (Fig. 5a), exhibiting high absorption across the solar spectrum (295–2500 nm) with minimal transmittance ($\approx$ 0%) and an exceptional photo-thermal conversion efficiency of up to 93.4%.[64] This innovative design maximizes the utilization of incoming sunlight for energy conversion. Similarly, Ito et al. designed a versatile porous graphene material with excellent heat localization and steam generation capabilities, achieving an impressive energy conversion rate of 80% through solar radiation (Fig. 5b).[65] These advancements highlight the potential of carbon-based materials in photothermal catalysis. However, one challenge associated with graphene sheets is the shading effect due to their light-blocking nature. This issue can be
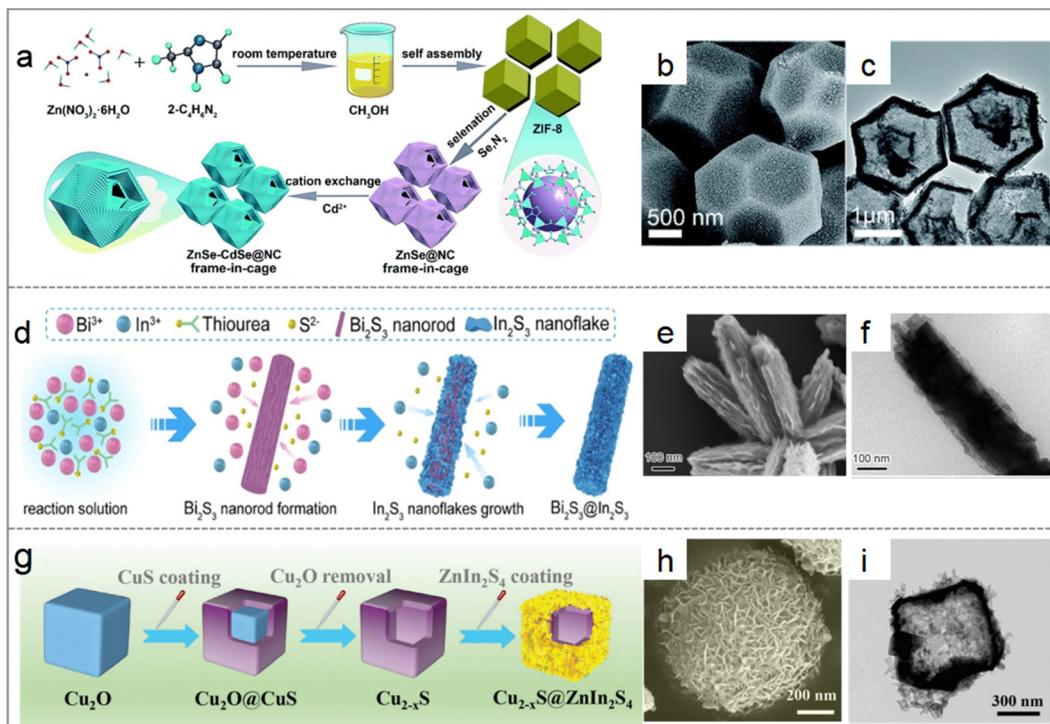
Fig. 4 Illustration of the preparation processes and micrographs of (a–c) ZnSe−CdSe@NC frame-in-cage,[59] (d–f) Bi_2S_3@In_2S_3,[60] and (g–i) $Cu_{2-x}S$@Z-nIn_2S_4 core−shell hollow nanoboxes.[61]
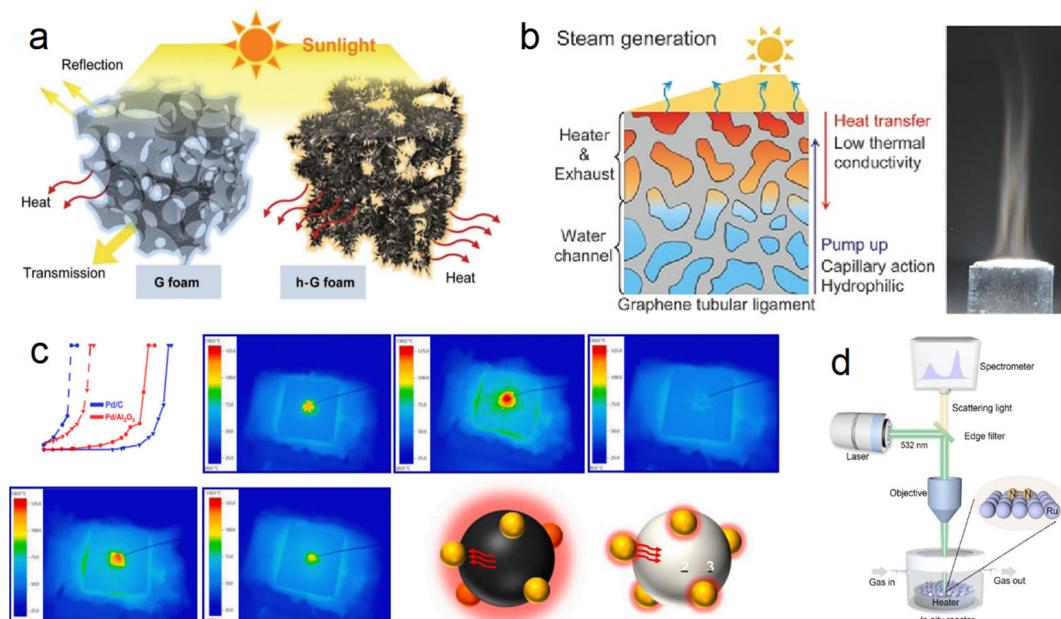

Fig. 5 (a) Difference in solar-thermal conversion processes between ordinary graphene foam and hierarchical graphene foam.[64] (b) Multifunctional nanoporous graphene converting solar illumination into high-energy steam.[65] (c) Heat transfer path in CO conversion proved by IR monitoring images (carbon support → Pd → Al_2O_3).[66] (d) Schematic illustration of the customized *in situ* Raman system.[67]

mitigated by controlling the dosage of graphene sheets and utilizing small-pore semiconductors or in-plane pore materials for structural adjustments, allowing for improved light exposure and efficient catalytic performance.

Although significant advancements have been made in the field of graphene-based photothermal catalysis, it is important to acknowledge that these materials still lag behind noble metal/oxide catalysts due to their weaker interactions with

reactants. However, carbon emerges as a promising candidate for exploring photothermal catalysis when utilized as both a catalyst support and a photothermal material with full-spectrum light absorption capabilities. Liu *et al.* synthesized a Pd/C catalyst using commercial carbon (XC-72R) as a catalyst support through a reduction and impregnation method and applied it in the photothermal catalytic oxidation of CO reaction.[66] The Pd/C catalyst demonstrated excellent light absorption ability, exhibiting significantly better catalytic performance under light conditions compared to dark conditions. Under a light intensity of 900 mW cm^2, the temperature for achieving 100% CO conversion (TF$_{100}$, furnace temperature) for the 1% Pd/C catalyst decreased from 146 to 30 °C, realizing complete CO conversion at room temperature (Fig. 5c). This exceptional catalytic performance is attributed to the ultra-high local temperature generated by the excellent photothermal conversion ability of carbon. Furthermore, infrared light was identified as the primary contributor to the improved catalytic performance. This work opens new possibilities for harnessing solar energy using carbon-based materials.

In a different study, Bian *et al.* measured the actual reaction temperature of photothermal synthesis of ammonia on carbon-supported Ru catalysts to quantify the contribution of thermal electrons, employing Le Chatelier's principle (Fig. 5d).[67] By excluding the local heating effect, they found that the activation energy of photothermal catalysis is significantly lower than that of thermal catalysis (54.9 kJ mol^{-1} compared to 126.0 kJ mol^{-1}). This reduction in activation energy is attributed to the phenomenon of hot electron injection, which lowers the energy barrier for N$_2$ dissociation and intermediate product hydrogenation. Additionally, the injection of hot electrons suppressed the methanation reaction of carbon carriers, resulting in excellent operational stability of the catalyst over 1000 hours.

3.2.3 MXenes. MXenes, a group of 2D transition-metal carbides and nitrides, hold great promise in various photothermal

applications, including cancer treatment, solar water desalination, solar photothermal electrodes, and light-driven actuators. These materials exhibit exceptional photothermal conversion properties by efficiently absorbing electromagnetic waves and displaying LSPR effects.[28] The incorporation of metal nanoparticles into MXenes further enhances photocatalytic processes by facilitating the transfer of LSPR-excited hot charge carriers to both the metal nanoparticles and adsorbed reactants. Additionally, the strong binding between metals and MXene supports improves the dispersion of metal species on the MXene surface. By utilizing MXenes with excellent photothermal properties as catalyst supports, the sunlight absorption and photothermal conversion efficiency of supported metal catalysts can be significantly enhanced.

For example, Wu *et al.* utilized a chemical stripping method to obtain two-dimensional Mo$_2$TiC$_2$ nanosheets, which were then functionalized with Ru clusters (Ru/Mo$_2$TiC$_2$) (Fig. 6a).[68] These MXene-supported clusters exhibited remarkable photothermal conversion performance, with the surface temperature of Ru/Mo$_2$TiC$_2$ rapidly reaching 360 °C within 30 seconds under sunlight. After 5 minutes of illumination, the CO production rate reached 3.9 mol g$_{Ru}^{-1}$ h^{-1}, accompanied by a CO selectivity of 90% (Fig. 6b and c). This achievement positions Ru/Mo$_2$TiC$_2$ as one of the most effective photothermal catalysts reported for the reverse water-gas shift (RWGS) reaction. Another advantage of MXene materials lies in their tunable optical, electronic, thermal, and surface properties, which can be adjusted by modifying their compositions, structures, and terminations. This inherent versatility expands the range of available MXene-based materials. Notably, recent work by Wu *et al.* demonstrated that two representative MXene materials, Nb$_2$C and Ti$_3$C$_2$, enhance the photothermal effect, thereby boosting the photothermal catalytic activity of Ni nanoparticles (Fig. 6e and f).[28]

3.2.4 MOFs. MOFs are three-dimensional networks constructed from metal ion nodes and organic ligands, exhibiting
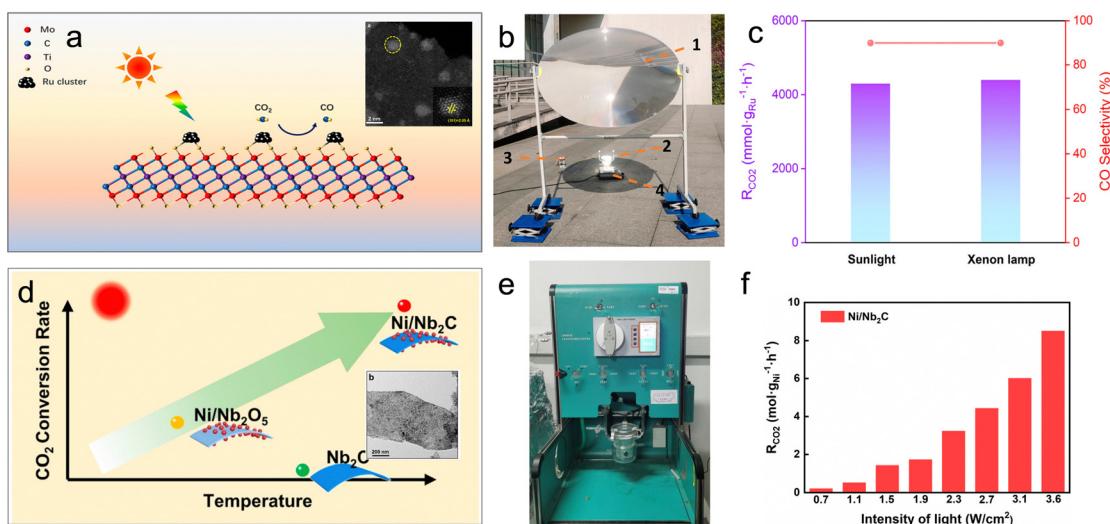
Fig. 6 (a) Schematic illustration and TEM image of the Ru/Mo$_2$TiC$_2$ photothermal catalyst. (b) Setup of the outdoor photothermal catalysis. (c) CO$_2$ conversion and product selectivity of Ru/Mo$_2$TiC$_2$ in photothermal catalytic RWGS.[68] (d) Schematic illustration and TEM image of the Ni/Ni$_2$C photothermal catalyst. (e) Photograph of the batch reactor. (f) Photothermal catalytic activity of Ni/Nb$_2$C in photothermal catalytic RWGS.[28]

semiconductor-like behaviors. The regularity, adjustable pore size, diverse topological structures, and malleability of MOFs make them promising materials for various catalytic reactions. While pure MOFs have limited active sites for photothermal catalytic conversion, they are commonly used as supports for photothermal catalysts in photothermal catalysis. The synthesis of the Pd nanocube (NC)@ZIF-8 composite has opened new avenues in catalytic research (Fig. 7a).[69] This innovative approach involves encapsulating Pd nanocubes into ZIF-8, resulting in a highly efficient and selective catalyst for hydrogenation reactions. The plasmonic photothermal effects of Pd nanocube cores convert light into heat, driving catalytic reactions. The ZIF-8 shell protects the Pd cores from oxidation and deactivation while also promoting catalytic hydrogenation through H_2 enrichment (Fig. 7b). The composite offers superior performance, including high selectivity and efficiency under irradiation conditions. Moreover, ZIF-8 functions as an 'insulator' for thermal management, reducing heat loss and enhancing catalyst performance. For instance, Zhang et al. developed a hybrid structure of Pt nanocubes and Au nanocages encapsulated in ZIF-8 (Au&Pt@ZIF).[70] Pt nanocubes act as catalysts, Au nanocages with strong extinction serve as solar conversion nanocrystals, and ZIF-8 functions as a 'heat insulator', preventing heat dissipation and forming a localized high-temperature area that significantly enhances the catalytic activity of Pt nanocubes under light irradiation (Fig. 7c). Recently, Chen et al. successfully fabricated a layered tubular structure of MOF-74 (Cu) by assembling nanosheet arrays, exhibiting remarkable photothermal catalytic properties for carbon dioxide conversion at room temperature under sunlight irradiation (Fig. 7d).[71] The MOF-74-HT material possesses abundant optical traps on its outer surface, nano-sized building blocks, and large accessible contact surface areas, synergistically enhancing photothermal effects and catalytic activity. The creation of such superstructures has the potential to revolutionize the field of pure MOFs, paving the way for innovative and multifunctional materials.

Overall, although semiconductor-based supports are widely used in photothermal catalyst applications, ongoing research aims to explore new materials and approaches to further advance this field.[36,72,73] In these approaches, heat energy is harnessed to drive catalytic reactions instead of being dissipated to the surrounding environment through convection and conduction. Through structural control, interface engineering, multifunctional assembly and nanoscale effects for meticulous selection and optimization of both the active component and support structure, researchers can develop highly efficient systems capable of catalyzing complex chemical transformations with exceptional precision and control. This continuous exploration and refinement of materials and strategies hold great promise for pushing the boundaries of photothermal catalysis and unlocking new possibilities in diverse areas of chemistry and beyond.

4. Photothermal catalytic C1 conversion using supported metal catalysts

When it comes to harnessing the power of solar energy, photothermal catalytic C1 chemistry has emerged as a highly promising alternative to traditional thermocatalysis. This innovative approach capitalizes on abundant and clean energy sources, and it has made remarkable progress in recent years. Over the past decade, significant advancements have been achieved in
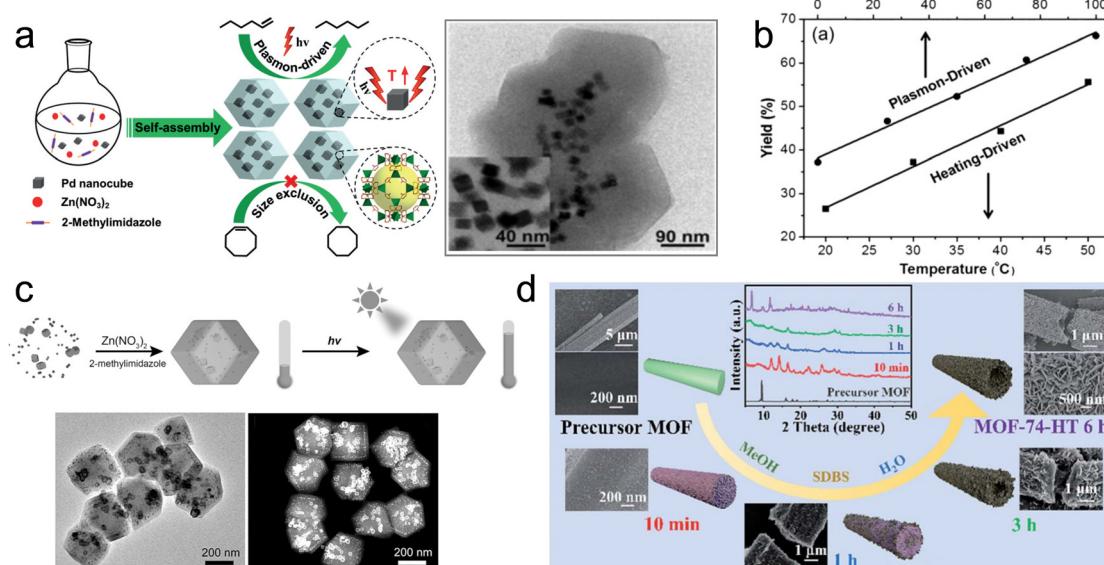
Fig. 7 (a) Self-assembly of Pd NCs@ZIF-8 and plasmon-driven selective catalysis of hydrogenation of olefins. (b) The hydrogenation performance of Pd NCs@ZIF-8.[69] (c) Schematic illustration of the formation of Au&Pt@ZIF and temperature variation under light irradiation.[70] (d) Phase transformation from the MOF precursor to MOF-74-HT.[71]

Table 1 Representative supported metal catalysts and their performances in photothermal catalytic C1 conversion

Catalysts	Reactant	Conversion/%	Products	Selectivity or mass specific activity	Ref.
Fe_5C_2/NC600	CO	22.3	C_{2-4}=	55.3%	75
Ni/MnO	CO	14.9	Light olefins	33%	76
Fe-500/ZnO–Al_2O_3	CO	20.9	Light olefins	42.4%	77
Co–Co_3O_4/ZnO–Al_2O_3	CO	15.4	Light olefins	36%	78
TiO_2-supported Ni_2P/Ni	CO	20.7	C_{2+}	70.7%	79
Ru_1Co-SAA	CO	58.6	C_{5+}	75.8%	80
Pt/α-MoC	CO	22	H_2		83
CuO_x/Al_2O_3	CO	>95	H_2		86
CeO_2/$Cu_{1.5}Mn_{1.5}O_4$	CO	96.6	H_2		87
$Ni_{12}P_5$/SiO_2	CO_2	960 ± 12 (mmol g_{cat}^{-1} h^{-1})	H_2	Near 100%	100
K^+–Co–C	CO_2	758 (mmol g_{cat}^{-1} h^{-1})	CO	99.8%	105
Ru–Al_2O_3 Rh–Al_2O_3 Ni–Al_2O_3	CO_2	95.75	CH_4	99.22%	38
Fe_3O_4 Fe_3C	CO_2	11.3 (mmol g_{cat}^{-1} h^{-1})	CO CH_4	100% 97%	42
Pd-loaded WN-WO_3	CO_2	40.6 ± 0.7 (mmol g_{cat}^{-1} h^{-1})	CH_4	100%	107
Ru–Al_2O_{3-x}-L	CO_2	87.68	CH_4	Near 100%	108
SA Ni/Y_2O_3	CO_2	80	CH_4	7.5 L m^{-2} h^{-1}	110
Au–Ru/TiO_2	CO_2		CH_4	99%	116
Fe/FeO_x supported on MgO–Al_2O_3	CO_2	50.1	C_{2+}	52.9%	117
AuCu–ZnO	CH_4		CH_3OH, CH_3OOH and HCHO	100%	120
Pd-def-In_2O_3	CH_4		CH_3OH and CH_3OOH	82.5%	121
Au/In_2O_3	CH_4		CH_3OH HCHO	97.62% 89.42%	122
Pt@BT-O	CH_4	8.2	propane	65%	123
Au/ZnO	CH_4		C_2H_6		124
TiO_2-supported Rh NPs	CH_4		CO_2, H_2		125
TiO_2-supported Pt	CH_4		H_2	185 (mmol g^{-1} h^{-1})	126
Single-layer Ni cluster stabilized by Al_2O_3	CH_4		CO H_2	9614.26 (mmol g_{Ni}^{-1} min^{-1}) 8572.96 (mmol g_{Ni}^{-1} min^{-1})	128
Ni/Ga_2O_3	CH_4		CO_2, H_2		129
Cu–Ru/MgO–Al_2O_3	CH_4		H_2	34 (mol mol_{Ru}^{-1} s^{-1})	130
Pt/CeO_2	CH_4		CO	22.7 (mmol g_{cat}^{-1} h^{-1})	131
Rh/Ce_xWO_3	CH_4		H_2 CO	88.5 (mmol g_{Rh}^{-1} h^{-1}) 152.3 (mmol g_{Rh}^{-1} h^{-1})	3

the field of photothermal catalytic C1 conversion. From improving photothermal catalytic CO conversion to groundbreaking developments in CO_2 hydrogenation, and conversions of methane and methanol, researchers are continuously pushing the boundaries of what can be accomplished with this transformative technology. The performance of supported catalysts for photothermal catalytic reactions in C1 chemistry has been summarized in Table 1. By harnessing the unique properties of light and heat, photothermal catalysis offers a more efficient and sustainable method for converting raw materials into valuable products. This exciting field holds immense potential for revolutionizing the energy landscape and enabling a more sustainable and greener future.

4.1 CO conversion

4.1.1 Fischer–Tropsch synthesis. Fischer–Tropsch synthesis (FTS) is a well-established method for converting syngas into fuels and chemicals, which has gained significant attention in light of declining oil resources and mounting environmental concerns.[74] In addition to its application in fuel synthesis, FTS can also be employed to produce light olefins (C_{2-4}=) from syngas, a process known as Fischer–Tropsch to olefins (FTO). Typically, harsh conditions (200–400 °C and 2–5 MPa) are required to lower the energy barrier for CO molecule activation and the C–C coupling process in the FTO process. However, solar-driven FTS has emerged as a promising alternative to conventional thermocatalytic FTS, as it enables operation under milder reaction conditions with lower energy requirements.

Recent studies have shown that Fe-based supported catalysts exhibit high selectivity for C_{2-4}= products and demonstrate excellent reaction activity in the FTO process. For instance, Ou's group synthesized a Fe_5C_2-loaded N-doped carbon microsphere catalyst (Fe_5C_2/NC600) using a wet chemistry method.[75] This catalyst exhibited broad sunlight absorption ability, exceptional C_{2-4}= selectivity of 55.3% (CO_2-free) at 22.3% CO conversion, and superior catalytic activity, which was 3.5 times higher than that of pristine Fe_5C_2 in the photothermal catalytic FTO process. Characterization techniques such as XPS, XAFS, CO-TPD, and CO pulse reaction revealed that pyrrolic N in the N-doped carbon support acted as an electron donor, transferring electrons to the surface of the active Fe_5C_2 phase and modifying its electronic structure. This electron transfer process created electron-rich active sites, enhancing the CO adsorption and dissociation ability of the Fe_5C_2-based catalyst, thereby increasing the CO conversion rate (Fig. 8a). The author further
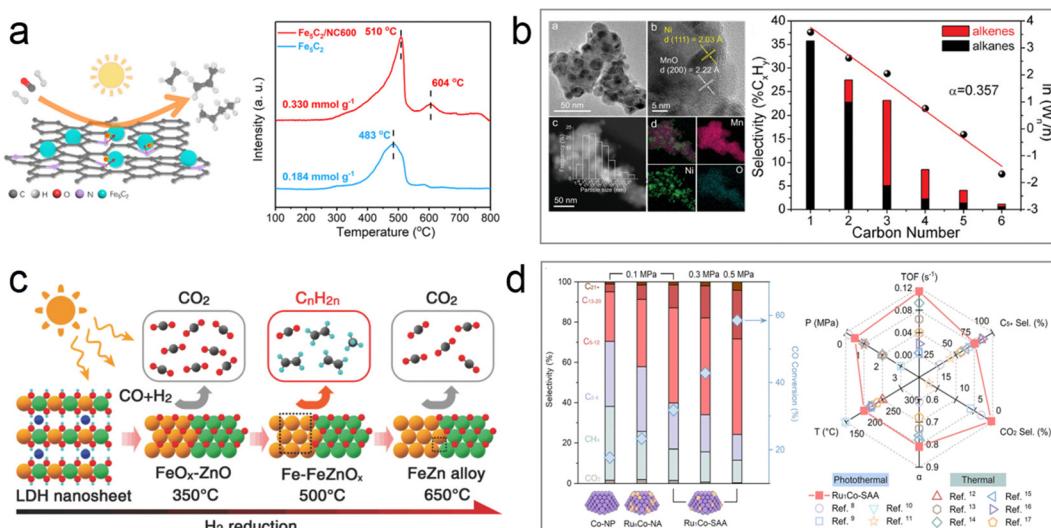
Fig. 8 (a) Scheme and CO adsorption ability of Fe_5C_2/NC600.[75] (b) Characterization data and product selectivity of the Ni/MnO catalyst.[76] (c) The CO hydrogenation selectivities of the Fe-x photocatalysts derived from ZnFeAl–LDH nanosheets at different temperatures.[77] (d) Comparison of FTS performance of Ru_1Co-SAA with other catalysts.[80]

investigated a series of Fe_5C_2-based catalysts with different supports (hydrophobic silica, hydrophilic silica, α-Al_2O_3, γ-Al_2O_3, and α,γ-Al_2O_3) *via* a one-step wet-chemical method to explore the influence of metal–support interaction on the photothermal catalytic FTO process. It was found that the weak interaction between the active phase and α-Al_2O_3 supports favored the formation of Fe_5C_2, contributing to high selectivity for light olefins.

Research on Ni-based catalysts for the photothermal FTO process has also been conducted. One study focused on developing Ni-containing nanoparticles supported on MnO catalysts (Ni/MnO) derived from the reduction of NiMn mixed metal oxide.[76] The optimized Ni/MnO catalyst with a Ni:Mn ratio of 2:1 demonstrated excellent performance in FTO, achieving a high selectivity of light olefins (33%) at 14.9% CO conversion under UV-visible light irradiation (Fig. 8b). Characterization techniques such as XAFS and XPS analysis of the Ni-500 catalyst revealed the presence of MnO-supported Ni nanoparticles, which induced modifications in the electronic structure and valence of the Ni nanoparticles, resulting in the formation of $Ni^{\delta+}$ sites. This slight change in nickel valence hindered the strong hydrogenation ability typically associated with Ni^0, leading to C–C coupling reactions that produced alkenes.

In one-step FTO processes, preventing the high selectivity for the by-product of CO_2 resulting from the WGS reaction remains a challenge. To address this issue, Zhang's group developed a series of Fe-based heterostructured photocatalysts by H_2 reduction of ZnFeAl–LDH precursor nanosheets at different temperatures (300–650 °C).[77] The Fe-500 catalyst (reduced at 500 °C), comprising Fe and FeO_x supported on ZnO and Al_2O_3, exhibited high selectivity (42%) for light olefins and low selectivity (11.4%) for CO_2 at a conversion of 20.9% in the photothermal FTO reaction. DFT calculations indicated that the abundant interface between Fe and FeO_x in the

Fe-500 heterostructured catalysts, along with moderate intermediate binding energies, contributed to the high selectivity for light olefins and suppressed CO_2 evolution (Fig. 8c). The author further investigated Co-based heterostructured catalysts derived from ZnCoAl–LDH precursor nanosheets.[78] Surprisingly, the Co–Co_3O_4/ZnO–Al_2O_3 catalyst exhibited high selectivity (36%) for light olefins at a CO conversion of 15.4%. The heterogeneous structure of oxide-modified metallic Co nanoparticles in this catalyst weakened the hydrogenation capacity of olefins, resulting in high selectivity for low carbon olefins.

In addition to light olefins, higher hydrocarbons (C_{2+}) are valuable products in the FTS process. Zhang *et al.* reported a partial phosphidation strategy for preparing TiO_2-supported Ni_2P/Ni heterostructure catalysts for photothermal FTS reactions.[79] Precise control over the degree of phosphating in Ni/Ni_2P catalysts was achieved by adjusting the input amount of NaH_2PO_2 during synthesis. The optimized Ni/Ni_2P-based catalyst for CO hydrogenation exhibited remarkable C_{2+} selectivity of 70.7% at a CO conversion rate of 20.7% under Xe lamp irradiation and demonstrated excellent stability in flow reaction system testing. DFT calculations indicated that metallic Ni facilitated CO activation, while Ni_2P/Ni favored C–C coupling. The coexistence of both metals provided an efficient pathway for CO hydrogenation to C_{2+} products, inhibiting over-hydrogenation to methane.

Metal alloys such as Fe, Co, Ni, and Ru can also achieve high CO conversion rates and selectivity for specific products. Zhang's group recently developed an Al_2O_3-supported RuCo single atom (Ru_1Co-SAA) catalyst derived from LDH topological transformation for converting syngas into C_{5+} liquid fuels *via* the photothermal catalytic FTS process.[80] Characterization of the Ru_1Co-SAA structure confirmed the successful preparation of isolated Ru atoms on the surface of metallic Co nanoparticles. The Ru_1Co-SAA catalyst exhibited higher CO conversion

activity (58.6%) and C_{5+} product selectivity (75.8%) compared to Al_2O_3-supported Co nanoparticles or RuCo nanoalloys (Fig. 8d). Furthermore, the FTS performance of Ru_1Co-SAA at low pressure was comparable to that of traditional FTS catalysts under higher pressure conditions. Chemisorption experiments and DFT calculations revealed that the Ru-Co coordination environment in Ru_1Co-SAA promoted CO dissociation and C–C coupling of CH_x^* intermediates while inhibiting H_2 activation and over-hydrogenation of CH_x^* intermediates. This promoted the effective growth of carbon chains to liquid products. This work is expected to inspire the design of more bimetallic catalysts for photothermal catalytic systems to convert small C1 molecules into high-value chemicals.

4.1.2 Water-gas shift reaction. The water-gas shift reaction (WGS: $CO + H_2O \rightarrow CO_2 + H_2$) plays a vital role in the modern chemical industry, which is highly significant, involving the conversion of CO and H_2O into CO_2 and H_2, making it essential for hydrogen production. To reduce energy consumption in H_2 production, researchers are actively seeking catalysts that efficiently activate water in the WGS reaction at low-temperature (below 250 °C).[81,82]

A recent study conducted by Zhang *et al.* presented a remarkable discovery regarding the activity of noble-metal Au clusters and Pt_1–Pt_n clusters on α-MoC in low-temperature WGS reactions, which achieved unprecedented rates of H_2 production (Fig. 9a).[83] However, the utilization of noble metals for large-scale H_2 production is impractical due to their high costs and the substantial amount of heat energy required from electricity or fossil fuel combustion. Consequently, it becomes crucial to prioritize the design and development of non-noble metal catalysts capable of activating water and efficiently driving WGS reactions using clean energy at lower temperatures. Previous research has demonstrated that semiconductor photocatalysts can drive the WGS reaction at room temperature when exposed to light irradiation. Nevertheless, the hydrogen production rates achieved through photocatalysis fall significantly below industry standards.[84–88]

In contrast, Cu-based photothermal catalysts for WGS have shown the ability to produce hydrogen at rates comparable to those of traditional high-temperature thermal catalysts when operated under light irradiation at 250–350 °C.[85,86,89,90] The group led by Ye reported that CuO_x/Al_2O_3 exhibits excellent catalytic activity (122 μmol g_{cat}^{-1} s^{-1} H_2 evolution and $>95\%$ CO conversion) in the solar-driven WGS process under light irradiation, surpassing noble-metal-based catalysts (Au/Al_2O_3 and Pt/Al_2O_3) in efficiency (Fig. 9b).[86] This solar-driven WGS process incurred no electric or thermal power costs while achieving 1.1% light-to-energy storage. However, the presence of an oxygen vacancy at the interface between Cu and Cu_2O in this catalyst limited reaction kinetics due to its singularity. To address this, CeO_2 was introduced as a promoter to facilitate oxygen transport from the H_2O reduction active site to that of CO, resulting in a low-CO-residual WGS reaction under H_2-rich conditions at a reaction temperature as low as 225 °C.[87] Photocarrier-enhanced photothermal catalysis over the CeO_2-loaded $Cu_{1.5}Mn_{1.5}O_4$ catalyst injects photocarriers into active sites and significantly reduces the apparent activation energy (decreased by 61%) (Fig. 9c).

However, it should be noted that photothermal catalysts for the WGS process exhibited inferior performance at temperatures below 250 °C when compared to thermal noble metal-based catalysts.[91–95] By leveraging the LSPR effects in metal nanoparticle-based catalysts, such as Au, Ag and Cu, it becomes possible to significantly lower the operating temperature of the WGS reaction. The LSPR excitation generated hot electrons from copper nanoparticles, which were then transferred to adsorbates like water molecules, leading to enhanced activation of these adsorbates. This approach showed promise in overcoming the high energy barrier for water dissociation, resulting in improved WGS reaction activity under mild conditions. Zhao *et al.* synthesized a novel LDH-derived Cu-based catalyst (LD-Cu) for photo-driven WGS reactions, consisting of Cu nanoparticles dispersed densely on an amorphous alumina
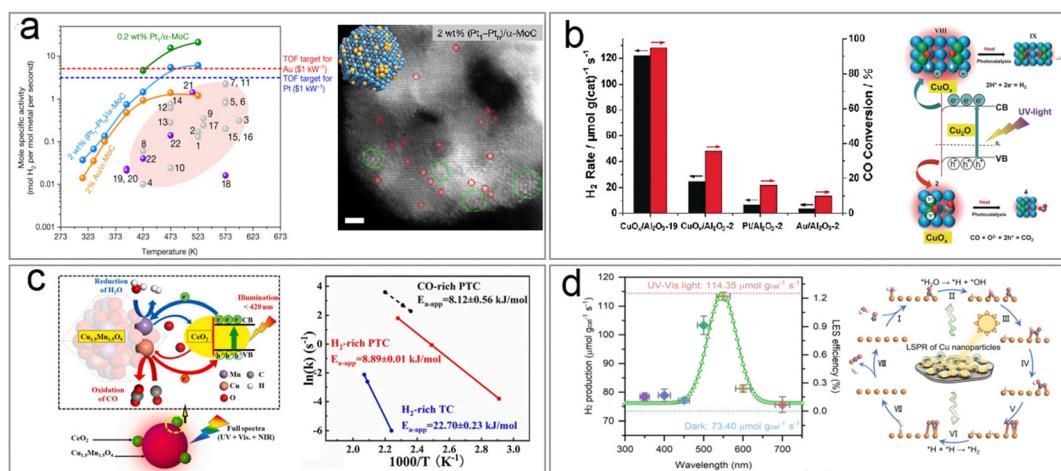

Fig. 9 (a) WGS performance and morphology of the Pt/α-MoC catalyst.[83] (b) WGS activity and mechanism of the CuO_x/Al_2O_3 catalyst.[86] (c) WGS reaction mechanism and the apparent activation energy of the $CeO_2/Cu_{1.5}Mn_{1.5}O_4$ catalyst.[87] (d) WGS reaction activity and mechanism of the LD-Cu catalyst.[96]

support (Fig. 9d).[96] Under UV/vis irradiation, LD-Cu exhibited excellent H_2 production activity at low temperatures (160–240 °C), significantly enhancing WGS reaction activity compared to tests conducted under dark conditions. Further experiments with monochromatic light sources revealed that the heightened H_2 production activity observed under UV/vis irradiation can be attributed to the excitation of LSPR in Cu nanoparticles, resulting in the generation of hot electrons. *In situ* diffuse reflectance Fourier transform infrared spectroscopy (DRIFTS) and DFT calculations further revealed that the light-induced LSPR effect promoted water activation and hydrogen generation. This study showcased the efficient driving of the WGS reaction at very low temperatures using plasmonic Cu nanoparticle-based catalysts, offering new possibilities for designing low-cost photo-driven catalysts for WGS reactions and other catalytic reactions requiring water activation.

4.2 CO_2 conversion

CO_2 capture and hydrogenation offer a promising approach to mitigate the greenhouse effect while simultaneously producing valuable chemicals. In addition to the product of CO, there is also interest in targeting methane, methanol, and higher carbon products (C_{2+}). However, the key challenge lies in developing suitable catalysts that can activate stable CO_2 molecules with high C=O bond energy while controlling the selectivity of the desired products.[97]

4.2.1 Reverse water-gas shift reaction.
One specific reaction of interest is the RWGS, which is the backward reaction of WGS reaction.[98,99] Recent studies have highlighted the effectiveness of metal phosphide materials as efficient photothermal catalysts for RWGS. For example, Xu *et al.* synthesized nanoparticles with a diameter of 86 nm by reducing nickel phosphate oxides under H_2 flow.[100] Additionally, SiO_2-supported $Ni_{12}P_5$ samples with varying loadings (3.1, 5.2, and 10.4 wt%) and different diameters (13, 9, and 8 nm) were prepared using wet impregnation. UV-vis-NIR spectra revealed

that the $Ni_{12}P_5$ nanoparticles exhibited broad absorption throughout the UV-vis-NIR region. However, the optical absorption decreased upon loading $Ni_{12}P_5$ on SiO_2 due to the dilution of the SiO_2 support. Among the samples, the 10.4 wt% $Ni_{12}P_5$/SiO_2 catalyst demonstrated the highest CO production rate (960 ± 12 mmol g_{cat}^{-1} h^{-1}), excellent selectivity (near 100%), and long-term stability (Fig. 10a–c). These attributes can be ascribed to the presence of enough exposed reaction sites with small particle size and favorable light-harvesting ability. Furthermore, photocatalytic experiments indicated that the catalyst absorbed incident photon flux and converted it into heat to drive subsequent catalytic reactions, distinguishing it from a photochemical process. *In situ* DRIFTS measurements and DFT calculations suggested that the P atoms in $Ni_{12}P_5$ effectively separated Ni atoms into highly dispersed nanoclusters, leading to reduced binding energy between Ni sites and CO molecules. Moreover, $Ni_{12}P_5$ nanoparticles exhibited exceptional light absorption ability across the entire sunlight spectrum, enhancing its photothermal catalytic activity and promoting RWGS reactions. Similar phenomena were observed in the Co_2P/SiO_2 system.[100]

The photothermal catalysts dispersed on high surface-area supports, such as Si,[101] Cu_2O,[47] CeO_2,[102] and Al_2O_3,[103] also showed sufficient exposure of active sites and better photothermal conversion efficiency. For example, Robatjazi *et al.* presented novel plasmon-mediated heterogeneous catalysts utilizing earth-abundant Al embedded in Cu_2O, which exhibit enhanced efficiency and selectivity for RWGS reaction under light illumination compared to conventional thermal conditions.[47] The plasmon resonance of Al generates more energetic hot-carriers and enhances the optical absorption in Cu_2O for selective conversion of CO_2 to CO under visible light irradiation (Fig. 10d). This work also demonstrates the potential application of plasma photothermal catalysts in energy conversion.

The utilization of low-density carbon materials as supports can enhance the active mass loading and significantly improve
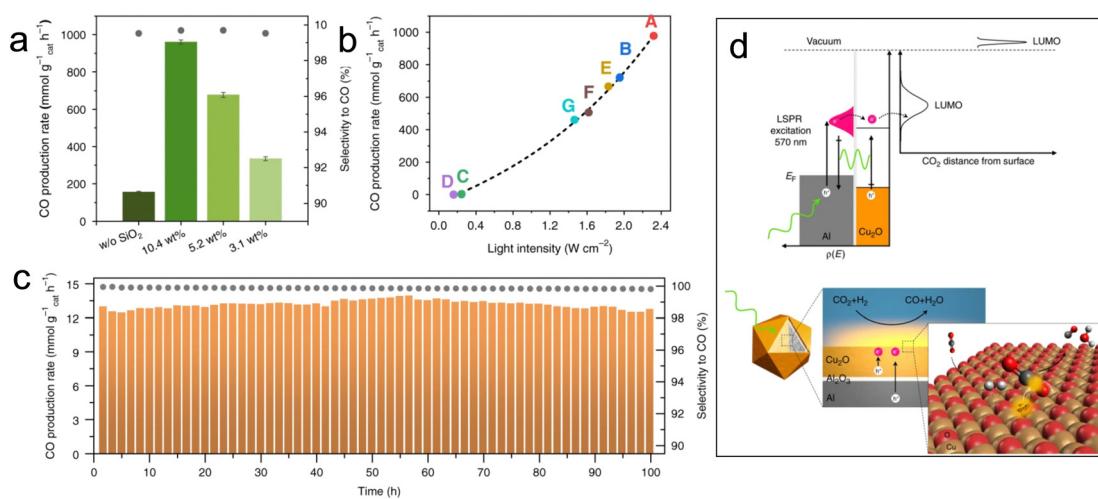
Fig. 10 (a) CO production rate, (b) selectivity, and (c) long-term stability of $Ni_{12}P_5$/SiO_2 catalyst in the photothermal RWGS reaction.[100] (d) Structure and mechanism of plasmon-induced carrier-assisted RWGS on Al@Cu_2O.[47]

the overall CO productivity.[104] Very recently, Wang *et al.* presented a potassium-modified carbon-supported cobalt (K$^+$–Co–C) catalyst that emulates the structure of a lotus pod.[105] As a result of the designed lotus-pod structure, which incorporated an efficient photothermal C substrate with hierarchical pores, an intimate Co/C interface featuring covalent bonding, and exposed Co catalytic sites exhibiting optimized CO binding strength, the K$^+$–Co–C catalyst exhibited exceptional performances in the photothermal RWGS reaction, achieving a record-breaking rate of 758 mmol g$_{cat}^{-1}$ h^{-1}, accompanied by an exceptional selectivity for CO at 99.8%, surpassing typical photochemical CO$_2$ reduction reactions by three orders of magnitude.

4.2.2 CO$_2$ methanation. Hydrogenation of CO$_2$ to methane, known as the Sabatier reaction, can proceed through different reaction pathways involving intermediate CO or formate species. Ye's group demonstrated the significant potential of group VIII metals (Ru, Rh, Ni, Co, Pd, Pt, Ir, and Fe) in enhancing the photothermal conversion of CO$_2$. Catalysts such as Ru–Al$_2$O$_3$, Rh–Al$_2$O$_3$, and Ni–Al$_2$O$_3$ exhibited reaction rates several orders of magnitude higher compared to other photocatalysts.[38] Another investigation by Ma's group focused on the selectivity of Fe-based oxides and Fe-based carbides for CO$_2$ hydrogenation products.[42] Fe$_3$O$_4$ exhibited 100% selectivity for CO production, while Fe$_3$C favored CH$_4$ production with 97% selectivity. By adjusting the carbonization conditions of the precursors, a series of iron base oxides and iron base carbides

can be prepared (Fig. 11a), allowing for a comparison of their selectivity in CO$_2$ hydrogenation products.

A recent development in the field involved a Pd-loaded WN-WO$_3$ heterostructure, which acted as a direct Z-scheme catalyst, broadening the absorption spectrum of solar energy for the photothermal-assisted conversion of CO$_2$ and H$_2$O into CH$_4$.[106] The catalytic activity reached 40.6 ± 0.7 mmol h^{-1} g^{-1} for CH$_4$ due to the unique carrier transfer mode of the Z-scheme catalyst. Under sunlight illumination, the WN-WO$_3$ heterostructure can efficiently separate and migrate photoinduced carriers, resulting in more energetic hot electrons involved in the reaction (Fig. 11b). The local photothermal effect facilitated the migration of gas molecules and carriers, thereby enhancing CO$_2$ conversion efficiency. Recent studies have also explored Ni nanoparticles supported on barium titanate perovskite for photothermal catalytic CO$_2$ conversion, achieving high CH$_4$ yields with nearly 100% selectivity. The dominant reactivity was attributed to a nonthermal hot-electron-driven pathway, aided by the local photothermal effect.[107]

To further advance photothermal catalytic CO$_2$ hydrogenation, the effect of SMSI has also been investigated. For instance, Ru–Al$_2$O$_{3-x}$-L, which is rich in defects, was grown *in situ* on aluminum foil using an ultraviolet pulsed laser, and then ultrasmall Ru nanoparticles were loaded in a controllable manner to prepare Ru–Al$_2$O$_{3-x}$-L, which achieved effective photothermal catalytic CO$_2$ methanation.[108] The willow fluff structured Al$_2$O$_{3-x}$-L can effectively capture light and ensure a high light
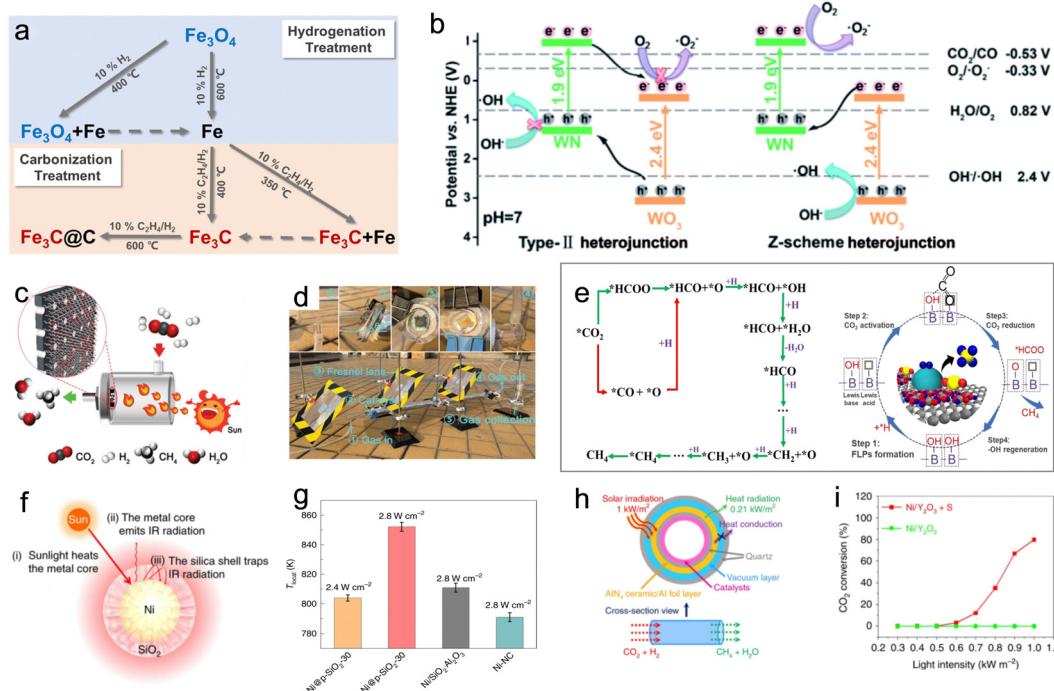
Fig. 11 (a) Preparation strategy for photothermal catalysts with varying degree of hydrogenation/carbonization.[42] (b) Schematic illustration of the charge-carrier migration mechanism according to the type-II and Z-scheme heterojunction for WN−WO$_3$.[106] (c) (d) Schematic illustration of the flow reactor system and outdoor flow reactor system for photothermal CO$_2$ methanation.[108] (e) The proposed reaction pathways and B(OH)$_x$ surface frustrated Lewis pair reaction pathway for CO$_2$ methanation.[109] (f) and (g) Schematic of the nanoscale greenhouse effect in Ni@p-SiO$_2$-30 and T_{local} of different catalysts under different illuminations.[103] (h) and (i) Schematic of the new photothermal catalytic CO$_2$ methanation system and the CO$_2$ conversion rates of the catalysts.[110]

adsorption capability of Ru–Al_2O_{3-x}-L. Defects in Al_2O_{3-x}-L serve as anchoring sites for Ru. The SMSI between the ultra-small Ru nanoparticles and Al_2O_{3-x}-L is established. An innovative flow reactor based on the one-piece Ru–Al_2O_{3-x}-L microchannel catalyst enhanced the CH_4 yield to 14.04 mol g_{Ru}^{-1} h^{-1} due to local pressure on the edge of the microchannels (Fig. 11c). In addition, the feasibility of photothermal catalytic CO_2 methanation (with a CH_4 yield of 18.00 mmol min^{-1}) was demonstrated through an outdoor setup (Fig. 11d). Zhu et al. reported a hexagonal boron nitride (h-BN) supported Ni particle (Ni/BN) as a photothermal catalyst for CO_2 methanation, showing excellent CO_2 conversion (87.68%), reaction rate (2.03 mol g_{Ni}^{-1} h^{-1}) and CH_4 production selectivity (near 100%) under ambient conditions.[109] During the photothermal-assisted oxidation operation, the photothermal effect of Ni particles generated higher temperatures at the BN interface than in other regions. This caused slight oxidation of the h-BN surface defect, leading to the formation of $B(OH)_x$ species (Fig. 11e). The B atom in $B(OH)_x$ underwent a transformation in its bonding, creating a normal covalent bond after losing its π-conjugated structure. The electron-deficient B^{3+} site, due to its nature, accepted electrons from O in CO_2, facilitated by the linear structure of the CO_2 molecule. This created an electron-deficient B^{3+} center (Lewis acid site) and OH (Lewis base site), forming a frustrated Lewis acid–base pair (HOB···B). This pair provided the appropriate energy for CO_2 adsorption and dissociation, serving as an activation site for photothermal catalytic methanation reactions. Furthermore, researchers have explored other exceptional photothermal supports, such as 2D MXenes. Wu et al. reported on Ni/Nb_2C catalysts supported by MXenes, which exhibited outstanding photothermal effects and achieved a record-breaking CO_2 conversion rate of 8.50 mol g_{Ni}^{-1} h^{-1} under 36 sun illumination, surpassing the reference of Ni/Nb_2O_5.[28]

In the realm of photothermal catalysis, the release of thermal radiation into the surrounding environment represents wasted heat energy. To address this issue, Cai et al. developed a catalyst composed of nickel nanocrystals encapsulated in nanoporous silica with 30 nm-thick shells, known as Ni@p-SiO_2.[103] This catalyst demonstrated superior photothermal catalytic efficiency for CO_2 hydrogenation (Fig. 11f). When exposed to light illumination at 2.8 W cm^{-2}, the Ni@p-SiO_2 catalyst reached a maximum temperature of 334 °C, as measured using a contacting thermocouple. In comparison, the reference catalysts (Ni/SiO_2·Al_2O_3 and Ni-NC) only achieved temperatures of 314 and 300 °C, respectively. These results highlight the enhanced photothermal catalytic efficiency conferred by the core–shell structure. As the thermocouple had limitations in precisely reflecting the local temperature (T_{local}) of the catalysts, the authors estimated T_{local} based on the gas composition under reaction equilibrium conditions. The findings revealed that Ni@p-SiO_2 exhibited the highest T_{local} of 852 K, further confirming its potent photothermal effect (Fig. 11g). This supraphotothermal phenomenon originated from the greenhouse-like engineering of the SiO_2 shell, which acted as both heat insulation and infrared shielding, minimizing heat loss

from the illuminated Ni inner region to the external surroundings. Due to its supra-photothermal and spatial confinement effects, the Ni@p-SiO_2 catalyst demonstrated improved photothermal catalytic performance and stability compared to Ni/SiO_2·Al_2O_3 and Ni-NC, enabling its activity in both CO_2 methanation and RWGS reactions.

In a different approach, Li et al. employed selective light absorbers to construct a photothermal system capable of generating high temperatures (up to 288 °C) under low solar exposure (1 kW m^{-2}).[110] This system exhibited three times higher efficiency than conventional photothermal catalytic systems (Fig. 11h). Moreover, ultra-thin amorphous Y_2O_3 nanosheets decorated with single nickel atoms (SA Ni/Y_2O_3) were synthesized and displayed superior activity in CO_2 methanation. With the aid of a selective light absorber, SA Ni/Y_2O_3 achieved an CO_2 conversion efficiency of 80% and a CH_4 production rate of 7.5 L m^{-2} h^{-1} under solar irradiation ranging from 0.52 to 0.7 kW m^{-2} (Fig. 11i). These results demonstrate the potential of SA Ni/Y_2O_3 as a platform for the direct conversion of dispersed solar energy into valuable chemicals.

4.2.3 Methanol production. Methanol, as a valuable feedstock for various organic chemical products, has spurred extensive research in the field of photothermal catalytic hydrogenation of CO_2 to methanol.[111] Among commercially available catalysts, Cu/ZnO/Al_2O_3 composites (60 wt% Cu, 30 wt% ZnO, and 10 wt% Al_2O_3) have shown promise for thermocatalytic CO_2 hydrogenation to methanol. To enhance the photothermal catalytic performance of Cu–ZnO based catalysts, numerous optimizations have been explored, capitalizing on the abundant active sites and SMSI at the Cu–ZnO interface.[112] In a study by Xie et al., the Cu/ZnO/Al_2O_3 catalyst was investigated under simultaneous thermal and optical activation to understand the interaction mechanism between electron excitation and surface chemical processes.[113] The findings revealed that UV or visible light irradiation-excited hot carriers facilitated the direct decomposition of CO_2 into CO, resulting in the formation of Cu(I)–O species on the Cu surface. Moreover, the transfer of hot electrons induced by LSPR from Cu to the adsorbate enhanced the reduction of Cu(I)–O species. Simultaneous excitation of both Cu and ZnO weakened the net electron transfer, thereby promoting surface reactions on ZnO (HCOO* hydrogenation) and Cu (H_2 cracking), leading to increased methanol production around the Cu–ZnO interface. Besides, the introduction of Mg and La into this catalyst introduced ZnO-based defects, effectively modulating the chemical interaction between Cu and ZnO and providing novel insights into the correlation between metal–support interaction at the interface and photochemical efficiency in the photoassisted methanol production process.[114]

4.2.4 Hydrocarbon production. While photothermal catalytic CO_2 hydrogenation has successfully produced C1 chemicals, there is a growing interest in synthesizing higher value-added C_{2+} hydrocarbon products.[115] Although significant progress has been made in obtaining C1–C3 hydrocarbons from CO_2 hydrogenation, more efficient methods are required

to produce these valuable compounds. Presently, most catalysts employed for multi-carbon generation necessitate noble metal supports, combinations of metallic elements and various oxide catalysts, or the construction of complex catalyst structures. However, recent studies have shown promising results in achieving C_{2+} hydrocarbons through photothermal catalytic approaches. For instance, a CoFe-based photothermal catalyst derived from layered double hydroxide has been observed to produce C_{2+} hydrocarbons (Fig. 12a).[46] Additionally, Zhang *et al.* reported a dual-functional Au–Ru/TiO$_2$ catalyst capable of decomposing H_2O to H_2 while hydrogenating CO_2, enabling the conversion of CO_2 and H_2O into fuels through photothermal coupling catalysis.[116] This study investigated thermocatalytic CO_2 hydrogenation, photothermal catalytic CO_2 hydrogenation, photothermal catalytic H_2O splitting to produce H_2, and photothermal catalytic reduction of CO_2 and H_2O. Au/TiO$_2$ exhibited high selectivity and productivity in thermocatalytic CO_2 hydrogenation, while Ru/TiO$_2$ demonstrated superior formation rates of CH_4 and C_2H_6. Although Au–Ru/TiO$_2$ shared similar

characteristics to Ru/TiO$_2$, its activity was slightly lower due to the partial blocking effect of Au. However, the production rates of CH_4 and C_2H_6 increased with temperature elevation. Under photothermal catalytic conversion of CO_2 and H_2, Au–Ru/TiO$_2$ exhibited significantly higher activities (Fig. 12b).

Recently, a Fe/FeO$_x$ heterogeneous structure supported on MgO–Al$_2$O$_3$ mixed metal oxide, derived from hydrogen reduction of the MgFeAl–LDH precursor, has also been employed for photothermal catalytic CO_2 hydrogenation.[117] The catalyst exhibited a surprising C_{2+} selectivity of 52.9% at a CO_2 conversion rate of 50.1% under UV-visible light irradiation. The coexistence of Fe and FeO$_x$ was found to be favorable for promoting the C–C coupling reaction, thereby enhancing the selectivity of C_{2+} products (Fig. 12c). Notably, there was no discernible difference in performance between photothermal catalysis and thermal catalysis processes for CO_2 hydrogenation to C_{2+}.

In another work, Ning *et al.* prepared a Co^0–$Co^{\delta+}$ structure catalyst through *in situ* photothermal activation. Co–CoO$_x$/MgAl$_2$O$_4$ achieved a C_{2-4} yield of 1303 μmol g^{-1} h^{-1} under light
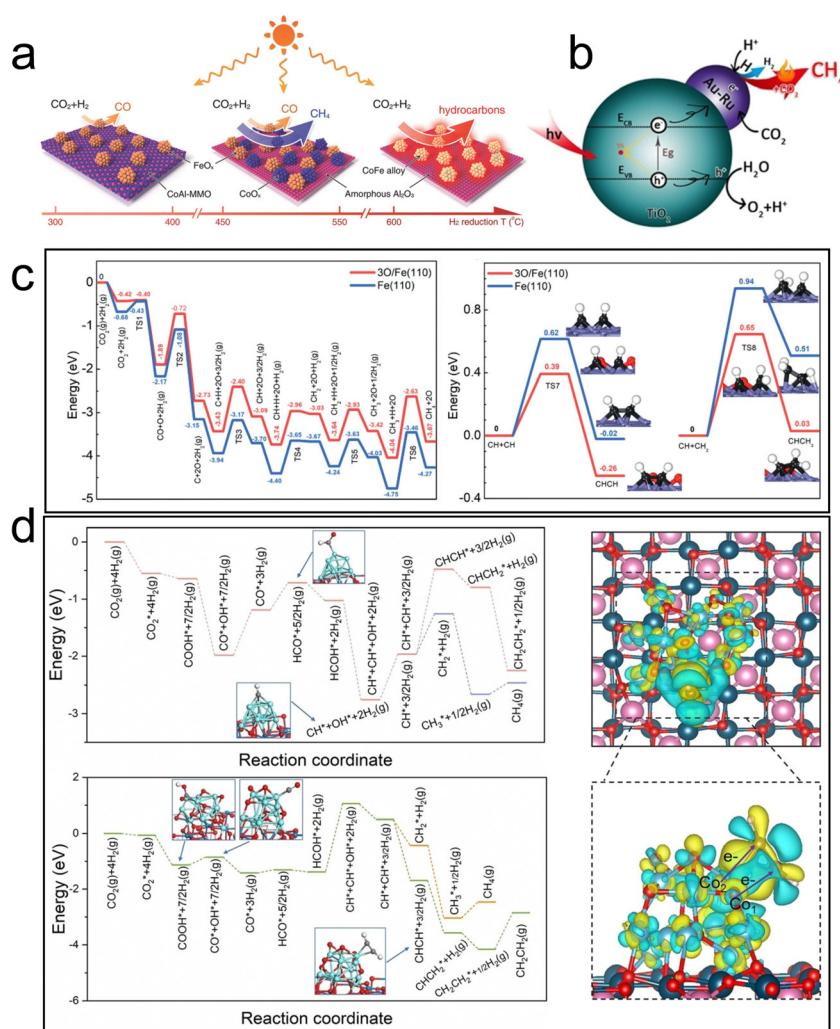

Fig. 12 (a) Illustration of selectivity in CO_2 hydrogenation over different CoFe-x catalysts.[46] (b) Coupling of thermocatalysis and photocatalysis in CO_2 hydrogenation over Au–Ru/TiO$_2$.[116] (c) Potential-energy profile of possible pathways for CO_2 conversion at active sites.[117] (d) C–C coupling mechanism of Co^0 and Co^0–$Co^{\delta+}$ over Co–CoO$_x$/MgAl$_2$O$_4$ by theoretical calculations.[118]

irradiation.[118] The selectivity of C_{2-4} total organic carbon reached 62.5%, and the ratio of olefin to alkane reached approximately 11. Experimental and theoretical results confirmed that the two active sites at the interface effectively adsorbed and activated CO_2 to form C1 intermediates through the Co^0 site. The introduction of the $Co^{\delta+}$ electron-deficient state effectively reduced the reaction energy of the key CHCH* intermediate, thus promoting the formation of low carbon olefin C_{2+} hydrocarbons (Fig. 12d). This study offers a novel approach to designing photothermal catalysts for the conversion of CO_2 to C_{2+} hydrocarbons through photoreduction.

4.3 Methane conversion

Methane, a colorless and odorless gas, serves as a vital building block in the chemical industry. It is primarily known for being the main component of natural gas and methane clathrates, which are found deep beneath the ocean floor. This versatile hydrocarbon feedstock plays a crucial role in the synthesis of fuels and other essential chemicals. The commercial production of H_2 heavily relies on catalytic steam reforming technology, along with partial oxidation and coal gasification methods. Therefore, it is evident that the conversion of CH_4 holds immense practical significance for the chemical industry.

4.3.1 Methane oxidation. Complete oxidation of methane (COM, $CH_4 + 2O_2 \rightarrow CO_2 + 2H_2O$) is thermodynamically favorable, but the resulting products have relatively low value compared to other chemical compounds. Partial oxidation of methane (POM) to value-added liquid commodities (like CH_3OH and HCHO, HCOOH, *etc.*) proves to be a more attractive option from a catalysis perspective.[119] Recently, Tang's group constructed AuCu–ZnO photothermal catalysts modified with highly dispersed two-site cocatalysts (AuCu), achieving a breakthrough in the quantum yield of methane conversion at room temperature, reaching 14.1% (365 nm) (Fig. 13a–d).[120] On the basis of this work, the authors utilized a Pd single atom cocatalyst and co-modified oxygen vacancies in a new indium oxide catalyst (Pd-def-In_2O_3), thereby extending the utilization range of the solar spectrum into visible region (Fig. 13e).[121] They achieved direct conversion of methane under 420 nm visible light irradiation, with the yield of carbon-liquid products reaching nearly 100 μmol h^{-1} and the primary product selectivity (CH_3OH and CH_3OOH) as high as 82.5%. Mechanistic studies revealed that Pd single atoms and oxygen vacancies acted as photogenerated holes and electron acceptors, respectively, synergistically promoting carriers' separation and transportation. Isotope experiments and electron paramagnetic resonance spectroscopy demonstrated that O_2 was the sole source of oxygen for methanol production, while H_2O generated hydroxyl radicals ($^{\bullet}OH$) through photogenerated hole activation, which then activated methane molecules (Fig. 13f).
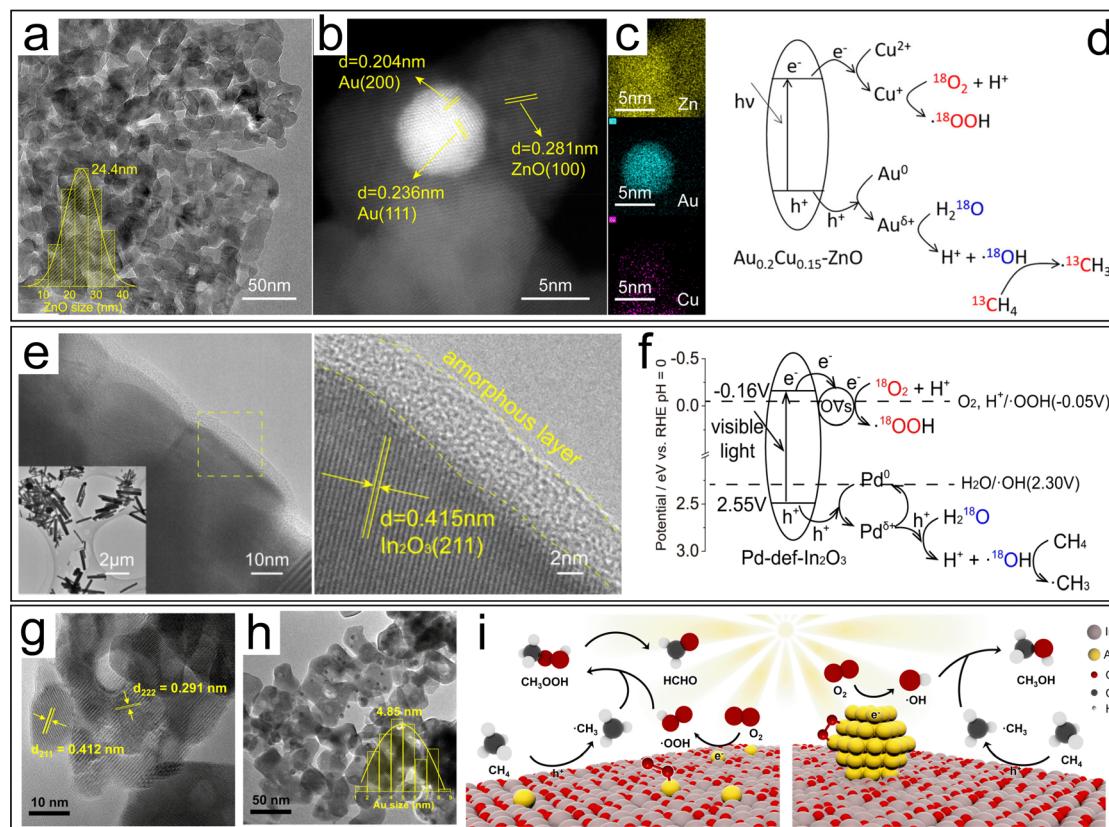
**Fig. 13** (a) TEM image of ZnO. (b) HAADF-STEM and (c) EDS-mapping images of $Au_{0.2}Cu_{0.15}$–ZnO. (d) Methane conversion mechanism of AuCu–ZnO.[120] (e) HRTEM images and (f) CH_4 conversion mechanism of Pd-def-In_2O_3.[121] TEM images of (g) Au_1/In_2O_3 and (h) AuNPs/In_2O_3. (i) Proposed mechanism of photocatalytic conversion of CH_4 to HCHO or CH_3OH on Au_1/In_2O_3 and AuNPs/In_2O_3, respectively.[122]

Very recently, Jiang *et al.* achieved high yields and selectivity for CH$_3$OH (6.09 mmol g^{-1}, 97.62%) and HCHO (5.95 mmol g^{-1}, 89.42%) by precisely controlling the efficient path of free radicals (•OOH and •OH) formed during the reaction process. They achieved this by adjusting the band structure of the semiconductor and controlling the size of the active site (either Au single atoms or Au nanoparticles) in the Au/In$_2$O$_3$ catalyst (Fig. 13g–i).[122]

4.3.2 Non-oxidative coupling of methane. Non-oxidative coupling of methane (NOCM) is an attractive reaction that directly converts methane to C$_{2+}$ and H$_2$. However, conventional catalytic NOCM processes face challenges due to the high stability of CH$_4$ molecules and the extremely strong C–H bond

energy, necessitating elevated temperatures for activation. Unfortunately, these high temperatures often lead to side reactions, such as coke formation and catalyst deactivation. The introduction of photocatalysts offers a promising solution by overcoming the CH$_4$ activation barrier, opening up new possibilities for this process. One notable example is Pt/black TiO$_2$ (Pt@BT-O) photothermal catalysts, which exhibited remarkable alkane dehydrogenation properties under near-infrared light and at room temperature (Fig. 14a and b).[123] The authors achieved a conversion rate of 8.2% of methane into propane with a selectivity of 65%, which is impressive considering that ethane is typically the dominant product. The proposed mechanism involves intramolecular dehydrogenation of methane, resulting
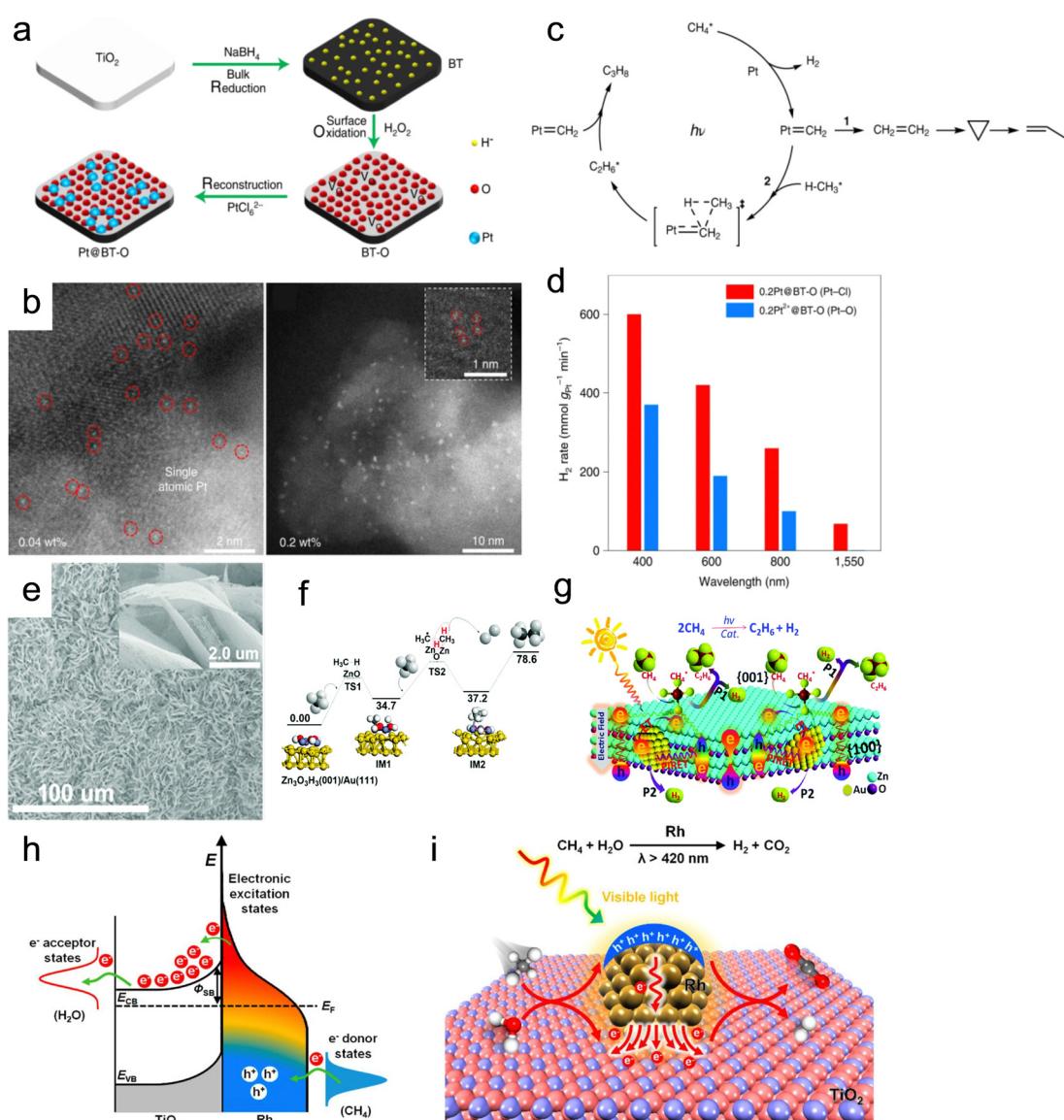

Fig. 14 (a) Synthesis and (b) characterization of the Pt@BT-O catalyst. (c) Proposed mechanism and (d) catalytic activity of catalysts for cyclohexane dehydrogenation.[123] (e) SEM image of the Au/ZnO photothermal catalyst. (f) Potential energy diagram for the methane coupling reaction on Zn$_3$O$_3$H$_3$(001)/Au(111) clusters. (g) Schematic description for the dehydrogenative coupling of methane into ethane over Au/ZnO.[124] (h) Schematic of energy transfer from photoexcited hot carriers to adsorbate states. (i) Mechanism description for the SRM reaction on Rh/TiO$_2$ under visible light illumination.[125]

in the formation of a methylene intermediate. The collective presence of closely positioned Pt species, rather than isolated Pt$^+$ monomers, contributed to enhanced photothermal catalytic activity and selectivity (Fig. 14c and d). Furthermore, Meng *et al.* reported a solar-to-C$_2$H$_6$ energy conversion efficiency of 0.08% on the polar surface of Au/ZnO porous nanosheets (Fig. 14e). This efficiency was achieved through the polarization and dissociation of methane C–H bonds by the local electric field normal to the polar plane, leading to the production of ethane and hydrogen *via* a radical coupling pathway (Fig. 14f). Mechanistic studies indicated that Au-plasmon-induced resonance energy transfer modulated the concentration of energetic charge carriers, initiating the stoichiometric conversion (Fig. 14g). The rate-determining step in methane coupling is the reduction of protons to H$_2$ by hot electrons.[124]

4.3.3 Steam reforming of methane. Steam reforming of methane, also known as SRM (SRM: CH$_4$ + H$_2$O → CO + 3H$_2$), is a highly utilized method for generating syngas that is employed for hydrogen production. The photothermal catalytic SRM process has become a topic of great interest among researchers in recent years, as it can operate at lower temperatures compared to traditional thermocatalytic methods. To delve deeper into the complexities of the SRM reaction, Ye's group investigated the influence of light on this process. To achieve this objective, they developed a prototype catalyst composed of TiO$_2$-supported Rh NPs.[125] They discovered that visible-light illumination had a significantly positive effect on CH$_4$ conversion at mild temperatures. Excited hot electrons from Rh NPs were rapidly transferred to the TiO$_2$ support, promoting water reduction and generating electron-deficient Rh species that exhibited high activity for CH$_4$ activation (Fig. 14h and i). Consequently, the apparent activation energy decreased by 50% compared to thermocatalytic processes. Under visible-light irradiation at 580 mW cm^{-2} and 280 °C, solar-to-fuel conversion efficiency was estimated to be 30.8%. The reduction of activation energy induced by light offers an effective and energy-efficient strategy. Han *et al.* demonstrated that the utilization of the black TiO$_2$-supported Pt catalyst can result in an exceptional rate of H$_2$ production during the SRM reaction. The experiment result revealed a remarkable production rate of 185 mmol h^{-1} g^{-1} under simulated sunlight irradiation at 500 °C.[126]

4.3.4 Dry reforming of methane. Photothermal catalytic dry reforming of methane (DRM: CH$_4$+ CO$_2$ → 2H$_2$ + 2CO) has emerged as an alternative to traditional thermal DRM, offering sustainable and low-temperature advantages. Extensive literature studies suggest that Ni-based catalysts are promising candidates for DRM in both thermal and photo-driven catalysis.[127] Recently, Hu *et al.* reported a unique nickel semi-metallic catalyst with a single-layer Ni cluster stabilized by Al$_2$O$_3$, exhibiting 100% atomic utilization efficiency and remarkable catalytic performance in photothermal DRM.[128] This catalyst demonstrated exceptionally high yields of H$_2$ and CO, reaching 8573.0 and 9614.3 mmol g$_{Ni}^{-1}$ min^{-1}, respectively, which were one order of magnitude higher than those for Ni nanoparticles. Moreover, the change in DRM kinetic process

inhibited the coke deposition, with no detectable coke formation observed. It was observed that light not only significantly improved the catalytic activity but also prevented rapid thermal catalytic deactivation by promoting the oxidation rate of carbon species and facilitating the desorption of strongly adsorbed CO$_2$ and CO.

Furthermore, the DRM process was hindered by a H$_2$/CO ratio of less than 1.0, primarily due to the simultaneous occurrence of the RWGS reaction. This reaction is not conducive to the formation of C$_{5-20}$ liquid fuels *via* FTS. Therefore, the regulation of the reaction paths to promote H$_2$ formation and suppress the RWGS reaction is a tremendous challenge. Zhou's group synthesized the Ni/Ga$_2$O$_3$ catalyst using a facile impregnation method.[129] The direction of electron transfer from the Ga$_2$O$_3$ support to Ni can be reversed under light irradiation, resulting in the formation of Ni^0 active sites. This generated abundant hot electrons through electronic interband transition of Ni, which enhanced H$_2$ formation and desorption. As a result, the H$_2$/CO ratio increased from 0.55 to 0.94 (Fig. 15a). Through *in situ* DRIFTS technology, it was discovered that light can promote the cracking of methane and accelerate the further cracking of methyl groups. Additionally, compared to thermal catalysis, photothermal catalysis resulted in a more significant reduction of methyl groups. Therefore, the introduction of light not only promoted methane pyrolysis but also facilitated continuous methyl group cracking. This study confirmed the non-thermal effects of light irradiation and the crucial role that light played in inducing directional electron migration.

In recent times, the integration of plasmonic 'antenna' metal nanoparticles with catalytically active 'reactor' materials has emerged as a remarkable strategy to enhance the efficiency, selectivity, and specificity of photocatalytic reactions. This innovative configuration harnesses the local optical field generated by the antenna to effectively convert the catalyst into a highly efficient photocatalyst. Zhou *et al.* synthesized a series of photothermal catalysts with different Ru loadings on the MgO–Al$_2$O$_3$ composite support by a coprecipitate method, and the impact of Ru concentration on the photothermal catalytic performance of Cu–Ru surface alloys was investigated, revealing that isolated Ru atoms on the Cu surfaces exhibited excellent DRM activity (Fig. 15b).[130] Through temperature programmed oxidation and thermal catalysis of isotopic reactants, it was determined that methane was the sole source of coke production. The authors speculated that CH$_4$ and CO$_2$ molecules first dissociated on the catalyst surface to form H^{ads}, C^{ads}, O^{ads} and CO^{ads}, respectively. The desorption of H$_2$ was accelerated by the hot carrier through the electron transition mechanism, which inhibited the reaction between H^{ads} and O^{ads}, leading to high photocatalytic selectivity. This inhibition can effectively promote the removal of carbon and improve the stability of the catalyst. In addition, H^{ads} was more likely to react with O^{ads} in the thermal catalytic process, and the lower decarbonization efficiency of O^{ads} led to lower selectivity and stability of the thermal catalytic reaction. The excellent photothermal catalytic performances with long term stability (50 h) and high selectivity (>99%) can be attributed to the light-excited hot carriers and single-atom active sites.
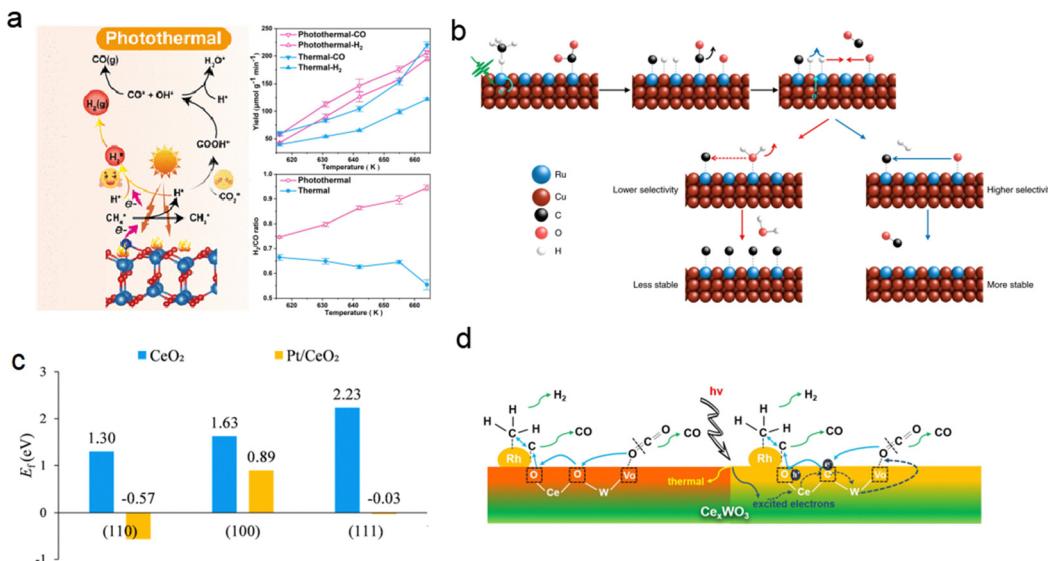
Fig. 15 (a) Schematic and DRM performance of the Ni/Ga$_2$O$_3$ catalyst.[129] (b) Schematic of enhanced selectivity and stability in Cu–Ru surface alloys.[130] (c) Oxygen vacancy formation energy of the Pt/CeO$_2$ catalyst.[131] (d) Schematic diagram for the light-driven DRM reaction over the Rh/Ce$_x$WO$_3$ catalyst.[3]

The construction of interfaces between single atoms and oxide catalysts with a synergistic effect has been proven to be effective in improving atomic utilization, reducing reaction energy consumption, and enhancing catalytic activity. For instance, the DRM reaction was catalyzed by a Pt monatomic catalyst supported by CeO$_2$ (Pt/CeO$_2$) with different morphologies at low temperature (300–450 °C).[131] Experimental and theoretical results demonstrated that rod-like CeO$_2$-R with abundant defects provided better anchoring for Pt monatoms, while Pt doping induced surface reconfiguration of CeO$_2$, significantly reducing the oxygen vacancy formation energy of CeO$_2$-R. The Pt–O lattice structure at the interface facilitated CH$_4$ oxygen-assisted dissociation, leading to CO formation through CH$_x$O intermediates. CO$_2$ was adsorbed and dissociated at the Pt–CeO$_2$ interface, generating CO and O lattice species to complete the catalytic cycle (Fig. 15c). Similar photo-induced redox cycles can occur in other heteronuclear bimetallic photocatalysts with oxygen bridging bonds. Yang *et al.* reported a highly active and coke-resistant DRM photocatalyst consisting of 3 nm Rh nanoparticles uniformly dispersed on Ce$_x$WO$_3$ nanosheets.[3] This catalyst utilized full-spectrum sunlight without the need for an external heat source and achieved a light-to-chemical energy efficiency of 4.65% under mild conditions. Metal-to-metal charge transfer induced by light facilitated the redox cycle, improving the catalyst's reaction activity and stability. Rapid oxygen migration assisted in the removal of carbon deposits and reduced the reaction start-up temperature. The authors attributed the catalyst's high performance, including H$_2$ and CO evolution rates of 88.5 and 152.3 mmol g$_{Rh}^{-1}$ h^{-1}, respectively, to the strong CO$_2$ absorption on the Ce$_x$WO$_3$ surface, the high mobility of oxygen and the electron transfer from Ce to W species (Fig. 15d). This construction of a heteronuclear bimetallic photocatalyst with oxo-bridge bonds provides valuable insights for the design of low-temperature DRM catalysts.

5. Summary and outlook

In summary, photothermal catalytic C1 chemistry offers a cleaner pathway for fuel synthesis using solar energy, which is particularly crucial in the face of climate change and the need for energy structure transformation. Supported catalysts with excellent optical properties and high specific surface area offer an ideal platform for photothermal catalysis. In this paper, we review the mechanism of photothermal catalysis, the design strategy for supported photothermal catalysts, and recent research progress in photothermal catalysis for C1 chemistry, including CO conversion (Fischer–Tropsch synthesis and water-gas-shift reaction), CO$_2$ conversion (reverse water-gas-shift reaction, methanation, methanol and higher hydrocarbon production), and methane conversion (oxidation, non-oxidative coupling, steam reforming, and dry reforming). Although significant progress has been made in the development of supported photothermal catalysts with excellent optical properties and high specific surface area, the field of photothermal catalysis is still in its early stages. Several challenges and prospects for future work can be identified:

(1) In order to further improve the performance of photothermal materials, it is still challenging to design materials with extremely high light absorption over a wide wavelength range, photothermal conversion ability, catalytic ability, and material stability. Advancements in this area are crucial to enable the cost-effective mass production of photothermal materials for everyday life and industrial applications.

(2) Distinguishing the differences between photocatalysis and thermal catalysis pathways in the context of photothermal processes is essential. Current temperature measurement methods, such as thermocouples or infrared cameras, provide macroscopic measurements but do not accurately reflect the local temperature of nanoparticles or fully capture the photothermal catalytic mechanism. Exploring new thermometry

technologies, such as scanning thermal microscopy (SThM) and non-contact measurement techniques based on Raman spectroscopy/*in situ* infrared spectroscopy, is necessary to achieve high sensitivity, accuracy, spectral/temporal resolution, reproducibility, stability, biocompatibility, cost-effectiveness, and ease of operation.

(3) By harnessing the power of light and heat, we can transform harmful gases like CO_2 and CH_4 into valuable polycarbon alkanes/olefins and other high-value chemicals. But this technology has even greater potential than just reducing emissions – it can also help us tackle industrial waste gases that would otherwise go unused. With further research and development, we can unlock a whole new world of possibilities for creating sustainable, profitable products from what was once considered waste.

Author contributions

Hui Liu: writing – original draft and investigation. Liangliang Han: investigation and writing – review and editing. Xiaoguang Duan: investigation. Hongqi Sun: supervision. Shaobin Wang: writing – review and editing and supervision. Jinqiang Zhang: writing – review and editing and supervision.

Conflicts of interest

There are no conflicts to declare.

Acknowledgements

References

1 Y. Liu, D. Deng and X. Bao, *Chem*, 2020, **6**, 2497–2514.

2 J. Bao, G. Yang, Y. Yoneyama and N. Tsubaki, *ACS Catal.*, 2019, **9**, 3026–3053.

3 Y. Yang, Z. Chai, X. Qin, Z. Zhang, A. Muhetaer, C. Wang, H. Huang, C. Yang, D. Ma, Q. Li and D. Xu, *Angew. Chem., Int. Ed.*, 2022, **61**, e202200567.

4 Q. Li, H. Wang, M. Zhang, G. Li, J. Chen and H. Jia, *Angew. Chem., Int. Ed.*, 2023, **62**, e202300129.

5 P. Tang, Q. Zhu, Z. Wu and D. Ma, *Energy Environ. Sci.*, 2014, **7**, 2580–2591.

6 S. Du, X. Bian, Y. Zhao, R. Shi and T. Zhang, *Chem. Res. Chin. Univ.*, 2022, **38**, 723–734.

7 H. W. Lin, S. N. Luo, H. B. Zhang and J. H. Ye, *Joule*, 2022, **6**, 294–314.

8 D. Mateo, J. L. Cerrillo, S. Durini and J. Gascon, *Chem. Soc. Rev.*, 2021, **50**, 2173–2210.

9 M. Fan, L. Cui, X. He and X. Zou, *Small Methods*, 2022, **6**, e2200855.

10 Y. Yang, S. Zhao, L. Cui, F. Bi, Y. Zhang, N. Liu, Y. Wang, F. Liu, C. He and X. Zhang, *Green Energy Environ.*, 2023, **8**, 654–672.

11 Y. Y. Li, Y. S. Zhang, K. Qian and W. X. Huang, *ACS Catal.*, 2022, **12**, 1268–1287.

12 Y. Zhao, W. Gao, S. Li, G. R. Williams, A. H. Mahadi and D. Ma, *Joule*, 2019, **3**, 920–937.

13 H. L. Wang, L. S. Zhang, Z. G. Chen, J. Q. Hu, S. J. Li, Z. H. Wang, J. S. Liu and X. C. Wang, *Chem. Soc. Rev.*, 2014, **43**, 5234–5244.

14 A. Fujishima and K. Honda, *Nature*, 1972, **238**, 37–38.

15 S. Q. Luo, X. H. Ren, H. W. Lin, H. Song and J. H. Ye, *Chem. Sci.*, 2021, **12**, 5701–5719.

16 X. M. Zhang, Y. L. Chen, R. S. Liu and D. P. Tsai, *Rep. Prog. Phys.*, 2013, **76**, 046401.

17 W. L. Barnes, A. Dereux and T. W. Ebbesen, *Nature*, 2003, **424**, 824–830.

18 C. Song, Z. Wang, Z. Yin, D. Xiao and D. Ma, *Chem Catal.*, 2022, **2**, 52–83.

19 C. Choi, F. Zhao, J. L. Hart, Y. Gao, F. Menges, C. L. Rooney, N. J. Harmon, B. Shang, Z. Xu, S. Suo, Q. Sam, J. J. Cha, T. Lian and H. Wang, *Angew. Chem., Int. Ed.*, 2023, **62**, e202302152.

20 B. Han, Y. L. Zhang, Q. D. Chen and H. B. Sun, *Adv. Funct. Mater.*, 2018, **28**, 1802235.

21 D. Meng, S. Yang, L. Guo, G. Li, J. Ge, Y. Huang, C. W. Bielawski and J. Geng, *Chem. Commun.*, 2014, **50**, 14345–14348.

22 G. K. Lim, Z. L. Chen, J. Clark, R. G. Goh, W. H. Ng, H. W. Tan, R. H. Friend, P. K. Ho and L. L. Chua, *Nat. Photonics*, 2011, **5**, 554–560.

23 M. Acik, G. Lee, C. Mattevi, M. Chhowalla, K. Cho and Y. Chabal, *Nat. Mater.*, 2010, **9**, 840–845.

24 J. Deng, J. Li, P. Chen, X. Fang, X. Sun, Y. Jiang, W. Weng, B. Wang and H. Peng, *J. Am. Chem. Soc.*, 2016, **138**, 225–230.

25 X. Huang, Q. Qian, X. Zhang, W. Du, H. Xu and Y. Wang, *Part. Part. Syst. Charact.*, 2013, **30**, 235–240.

26 C. Maggi, F. Saglimbeni, M. Dipalo, F. De Angelis and R. Di Leonardo, *Nat. Commun.*, 2015, **6**, 7855.

27 C. X. Guo, X. J. Ma and B. Wang, *Acta Chim. Sin.*, 2021, **79**, 967–985.

28 Z. Wu, C. Li, Z. Li, K. Feng, M. Cai, D. Zhang, S. Wang, M. Chu, C. Zhang, J. Shen, Z. Huang, Y. Xiao, G. A. Ozin, X. Zhang and L. He, *ACS Nano*, 2021, **15**, 5696–5705.

29 W. Feng, X. Han, R. Wang, X. Gao, P. Hu, W. Yue, Y. Chen and J. Shi, *Adv. Mater.*, 2019, **31**, 1805919.

30 K. Hantanasirisakul and Y. Gogotsi, *Adv. Mater.*, 2018, **30**, 1804779.

31 M. M. Gao, T. X. Zhang and G. W. Ho, *Nano Res.*, 2022, **15**, 9985–10005.

32 F. Wang, C. Li, H. Chen, R. Jiang, L. D. Sun, Q. Li, J. Wang, J. C. Yu and C. H. Yan, *J. Am. Chem. Soc.*, 2013, **135**, 5588–5601.

33 J. T. Li, S. K. Cushing, F. K. Meng, T. R. Senty, A. D. Bristow and N. Q. Wu, *Nat. Photonics*, 2015, **9**, 601–607.

34 S. Linic, P. Christopher and D. B. Ingram, *Nat. Mater.*, 2011, **10**, 911–921.

35 H. An, M. Li, R. Liu, Z. Gao and Z. Yin, *Chem. Eng. J.*, 2020, **382**, 122953.

36 P. G. O'Brien, A. Sandhel, T. E. Wood, A. A. Jelle, L. B. Hoch, D. D. Perovic, C. A. Mims and G. A. Ozin, *Adv. Sci.*, 2014, **1**, 1400001.

37 H. Liu, X. Meng, T. D. Dao, H. Zhang, P. Li, K. Chang, T. Wang, M. Li, T. Nagao and J. Ye, *Angew. Chem.*, 2015, **127**, 11707–11711.

38 X. Meng, T. Wang, L. Liu, S. Ouyang, P. Li, H. Hu, T. Kako, H. Iwai, A. Tanaka and J. Ye, *Angew. Chem., Int. Ed.*, 2014, **53**, 11478–11482.

39 Z. Yang, T. Zhao, Y. Tang, Y. Jiang, H. Kitagawa, X. Wen and F. Wang, *J. Catal.*, 2023, **424**, 22–28.

40 Y. Guo, Y. Huang, B. Zeng, B. Han, M. Akri, M. Shi, Y. Zhao, Q. Li, Y. Su, L. Li, Q. Jiang, Y. T. Cui, L. Li, R. Li, B. Qiao and T. Zhang, *Nat. Commun.*, 2022, **13**, 2648.

41 Y. Zhao, Y. Wei, X. Wu, H. Zheng, Z. Zhao, J. Liu and J. Li, *Appl. Catal., B*, 2018, **226**, 360–372.

42 C. Song, X. Liu, M. Xu, D. Masi, Y. Wang, Y. Deng, M. Zhang, X. Qin, K. Feng, J. Yan, J. Leng, Z. Wang, Y. Xu, B. Yan, S. Jin, D. Xu, Z. Yin, D. Xiao and D. Ma, *ACS Catal.*, 2020, **10**, 10364–10374.

43 T. Fujita, K. Higuchi, Y. Yamamoto, T. Tokunaga, S. Arai and H. Abe, *Metals*, 2017, **7**, 406.

44 X. Liu, H. Shi, X. Meng, C. Sun, K. Zhang, L. Gao, Y. Ma, Z. Mu, Y. Ling and B. Cheng, *Sol. RRL*, 2021, **5**, 2100185.

45 B.-H. Lee, S. Park, M. Kim, A. K. Sinha, S. C. Lee, E. Jung, W. J. Chang, K.-S. Lee, J. H. Kim and S.-P. Cho, *Nat. Mater.*, 2019, **18**, 620–626.

46 G. Chen, R. Gao, Y. Zhao, Z. Li, G. I. N. Waterhouse, R. Shi, J. Zhao, M. Zhang, L. Shang, G. Sheng, X. Zhang, X. Wen, L. Z. Wu, C. H. Tung and T. Zhang, *Adv. Mater.*, 2018, **30**, 1704663.

47 H. Robatjazi, H. Zhao, D. F. Swearer, N. J. Hogan, L. Zhou, A. Alabastri, M. J. McClain, P. Nordlander and N. J. Halas, *Nat. Commun.*, 2017, **8**, 27.

48 M. Moliner, J. E. Gabay, C. E. Kliewer, R. T. Carr, J. Guzman, G. L. Casty, P. Serna and A. Corma, *J. Am. Chem. Soc.*, 2016, **138**, 15743–15750.

49 Z. Li, R. Yu, J. Huang, Y. Shi, D. Zhang, X. Zhong, D. Wang, Y. Wu and Y. Li, *Nat. Commun.*, 2015, **6**, 8248.

50 S. Wei, A. Li, J. C. Liu, Z. Li, W. Chen, Y. Gong, Q. Zhang, W. C. Cheong, Y. Wang, L. Zheng, H. Xiao, C. Chen, D. Wang, Q. Peng, L. Gu, X. Han, J. Li and Y. Li, *Nat. Nanotechnol.*, 2018, **13**, 856–861.

51 Z. Zhu, X. Hu, X. An, M. Xiao, L. Zhang, C. Li and L. He, *Chem. – Asian J.*, 2022, **17**, e202200993.

52 W. Wei, Z. Wei, R. Li, Z. Li, R. Shi, S. Ouyang, Y. Qi, D. L. Philips and H. Yuan, *Nat. Commun.*, 2022, **13**, 3199.

53 M. N. Ha, G. Lu, Z. Liu, L. Wang and Z. Zhao, *J. Mater. Chem. A*, 2016, **4**, 13155–13165.

54 L. Wang, Y. Wang, Y. Cheng, Z. Liu, Q. Guo, M. N. Ha and Z. Zhao, *J. Mater. Chem. A*, 2016, **4**, 5314–5322.

55 Y. Li, M. Wen, Y. Wang, G. Tian, C. Wang and J. Zhao, *Angew. Chem., Int. Ed.*, 2021, **60**, 910–916.

56 Y. Yang, S. Zhao, F. Bi, J. Chen, Y. Wang, L. Cui, J. Xu and X. Zhang, *Appl. Catal., B*, 2022, **315**, 121550.

57 C. Gao, Q. Meng, K. Zhao, H. Yin, D. Wang, J. Guo, S. Zhao, L. Chang, M. He and Q. Li, *Adv. Mater.*, 2016, **28**, 6485–6490.

58 Z. Shi, L. Lan, Y. Li, Y. Yang, Q. Zhang, J. Wu, G. Zhang and X. Zhao, *ACS Sustainable Chem. Eng.*, 2018, **6**, 16503–16514.

59 W. Han, Y. Chen, Y. Jiao, S. Liang, W. Li and G. Tian, *J. Mater. Chem. A*, 2022, **10**, 17642–17651.

60 K. Yan, D. Wu, T. Wang, C. Chen, S. Liu, Y. Hu, C. Gao, H. Chen and B. Li, *ACS Catal.*, 2023, **13**, 2302–2312.

61 Y. Wang, M. Liu, C. Wu, J. Gao, M. Li, Z. Xing, Z. Li and W. Zhou, *Small*, 2022, **18**, e2202544.

62 X. M. Gao, H. B. He, W. Zhu, C. M. Yang, K. X. Xu, B. B. Feng, Y. A. Hu and F. Fu, *Small*, 2023, **19**, 2206225.

63 J. U. Kim, S. Lee, S. J. Kang and T. I. Kim, *Nanoscale*, 2018, **10**, 21555–21574.

64 H. Ren, M. Tang, B. Guan, K. Wang, J. Yang, F. Wang, M. Wang, J. Shan, Z. Chen, D. Wei, H. Peng and Z. Liu, *Adv. Mater.*, 2017, **29**, 1702590.

65 Y. Ito, Y. Tanabe, J. Han, T. Fujita, K. Tanigaki and M. Chen, *Adv. Mater.*, 2015, **27**, 4302–4307.

66 Z. Liu, L. Niu, X. Zong, L. An, D. Qu, X. Wang and Z. Sun, *Appl. Catal., B*, 2022, **313**, 121439.

67 X. Bian, Y. Zhao, G. I. N. Waterhouse, Y. Miao, C. Zhou, L.-Z. Wu and T. Zhang, *Angew. Chem., Int. Ed.*, 2023, **135**, e202304452.

68 Z. Wu, J. Shen, C. Li, C. Zhang, K. Feng, Z. Wang, X. Wang, D. M. Meira, M. Cai, D. Zhang, S. Wang, M. Chu, J. Chen, Y. Xi, L. Zhang, T. K. Sham, A. Genest, G. Rupprechter, X. Zhang and L. He, *ACS Nano*, 2022, **17**, 1550–1559.

69 Q. Yang, Q. Xu, S. H. Yu and H. L. Jiang, *Angew. Chem., Int. Ed.*, 2016, **55**, 3685–3689.

70 W. Zhang, L. Wang, K. Wang, M. U. Khan, M. Wang, H. Li and J. Zeng, *Small*, 2017, **13**, 1602583.

71 H. Chen, L. Shao, C. Wang and Y. Fu, *J. Mater. Chem. A*, 2022, **10**, 17434–17439.

72 X. Feng, D. Liu, B. Yan, M. Shao, Z. Hao, G. Yuan, H. Yu and Y. Zhang, *Angew. Chem., Int. Ed.*, 2021, **133**, 18700–18704.

73 Q. Chen, Z. Pei, Y. Xu, Z. Li, Y. Yang, Y. Wei and Y. Ji, *Chem. Sci.*, 2018, **9**, 623–628.

74 M. E. Dry, *Catal. Today*, 2002, **71**, 227–241.

75 R. Li, Y. Li, Z. Li, W. Wei, Q. Hao, Y. Shi, S. Ouyang, H. Yuan and T. Zhang, *ACS Catal.*, 2022, **12**, 5316–5326.

76 Y. Wang, Y. Zhao, J. Liu, Z. Li, G. I. N. Waterhouse, R. Shi, X. Wen and T. Zhang, *Adv. Energy Mater.*, 2019, **10**, 1902860.

77 Y. Zhao, Z. Li, M. Li, J. Liu, X. Liu, G. I. N. Waterhouse, Y. Wang, J. Zhao, W. Gao, Z. Zhang, R. Long, Q. Zhang, L. Gu, X. Liu, X. Wen, D. Ma, L. Z. Wu, C. H. Tung and T. Zhang, *Adv. Mater.*, 2018, **30**, 1803127.

78 Z. Li, J. Liu, Y. Zhao, G. I. N. Waterhouse, G. Chen, R. Shi, X. Zhang, X. Liu, Y. Wei, X. D. Wen, L. Z. Wu, C. H. Tung and T. Zhang, *Adv. Mater.*, 2018, **30**, 1800527.

79 Z. Li, X. Zhang, J. Liu, R. Shi, G. I. N. Waterhouse, X. D. Wen and T. Zhang, *Adv. Mater.*, 2021, **33**, e2103248.

80 J. Zhao, J. Liu, Z. Li, K. Wang, R. Shi, P. Wang, Q. Wang, G. I. N. Waterhouse, X. Wen and T. Zhang, *Nat. Commun.*, 2023, **14**, 1909.

81 J. A. Rodriguez, S. Ma, P. Liu, J. Hrbek, J. Evans and M. Perez, *Science*, 2007, **318**, 1757–1760.

82 J. A. Rodriguez, P. Liu, J. Hrbek, J. Evans and M. Perez, *Angew. Chem., Int. Ed.*, 2007, **46**, 1329–1332.

83 X. Zhang, M. Zhang, Y. Deng, M. Xu, L. Artiglia, W. Wen, R. Gao, B. Chen, S. Yao, X. Zhang, M. Peng, J. Yan, A. Li, Z. Jiang, X. Gao, S. Cao, C. Yang, A. J. Kropf, J. Shi, J. Xie, M. Bi, J. A. van Bokhoven, Y. W. Li, X. Wen, M. Flytzani-Stephanopoulos, C. Shi, W. Zhou and D. Ma, *Nature*, 2021, **589**, 396–401.

84 L. Millard and M. Bowker, *J. Photochem. Photobiol., A*, 2002, **148**, 91–95.

85 Z. Zhang, S. S. Wang, R. Song, T. Cao, L. Luo, X. Chen, Y. Gao, J. Lu, W. X. Li and W. Huang, *Nat. Commun.*, 2017, **8**, 488.

86 L. Zhao, Y. Qi, L. Song, S. Ning, S. Ouyang, H. Xu and J. Ye, *Angew. Chem., Int. Ed.*, 2019, **131**, 7790–7794.

87 Y. Tong, L. Song, S. Ning, S. Ouyang and J. Ye, *Appl. Catal., B*, 2021, **298**, 120551.

88 S. M. Fang, B. H. Chen and J. White, *J. Phys. Chem.*, 1982, **86**, 3126–3130.

89 F. Liu, L. Song, S. Ouyang and H. Xu, *Catal. Sci. Technol.*, 2019, **9**, 2125–2131.

90 C. Shi, D. Yuan, L. Ma, Y. Li, Y. Lu, L. Gao, X. San, S. Wang and G. Fu, *J. Mater. Chem. A*, 2020, **8**, 19467–19472.

91 S. Yao, X. Zhang, W. Zhou, R. Gao, W. Xu, Y. Ye, L. Lin, X. Wen, P. Liu and B. Chen, *Science*, 2017, **357**, 389–393.

92 N. Liu, M. Xu, Y. Yang, S. Zhang, J. Zhang, W. Wang, L. Zheng, S. Hong and M. Wei, *ACS Catal.*, 2019, **9**, 2707–2717.

93 L. Sun, J. Xu, X. Liu, B. Qiao, L. Li, Y. Ren, Q. Wan, J. Lin, S. Lin, X. Wang, H. Guo and T. Zhang, *ACS Catal.*, 2021, **11**, 5942–5950.

94 N. Yi, R. Si, H. Saltsburg and M. Flytzani-Stephanopoulos, *Energy Environ. Sci.*, 2010, **3**, 831–837.

95 N. M. Schweitzer, J. A. Schaidle, O. K. Ezekoye, X. Pan, S. Linic and L. T. Thompson, *J. Am. Chem. Soc.*, 2011, **133**, 2378–2381.

96 J. Zhao, Y. Bai, Z. Li, J. Liu, W. Wang, P. Wang, B. Yang, R. Shi, G. I. Waterhouse and X. D. Wen, *Angew. Chem., Int. Ed.*, 2023, **62**, e202219299.

97 J. Zhao, R. Shi, G. I. N. Waterhouse and T. Zhang, *Nano Energy*, 2022, **102**, 107650.

98 J. Yu, A. Muhetaer, X. Gao, Z. Zhang, Y. Yang, Q. Li, L. Chen, H. Liu and D. Xu, *Angew. Chem., Int. Ed.*, 2023, **62**, e202303135.

99 M. Gonzalez-Castano, B. Dorneanu and H. Arellano-Garcia, *React. Chem. Eng.*, 2021, **6**, 954–976.

100 Y. F. Xu, P. N. Duchesne, L. Wang, A. Tavasoli, A. A. Jelle, M. Xia, J. F. Liao, D. B. Kuang and G. A. Ozin, *Nat. Commun.*, 2020, **11**, 5149.

101 X. Shen, C. Li, Z. Wu, R. Tang, J. Shen, M. Chu, A.-B. Xu, B. Zhang, L. He and X. Zhang, *Nanoscale*, 2022, **14**, 11568–11574.

102 B. Deng, H. Song, K. Peng, Q. Li and J. Ye, *Appl. Catal., B*, 2021, **298**, 120519.

103 M. Cai, Z. Wu, Z. Li, L. Wang, W. Sun, A. A. Tountas, C. Li, S. Wang, K. Feng, A.-B. Xu, S. Tang, A. Tavasoli, M. Peng, W. Liu, A. S. Helmy, L. He, G. A. Ozin and X. Zhang, *Nat. Energy*, 2021, **6**, 807–814.

104 S. Ning, H. Xu, Y. Qi, L. Song, Q. Zhang, S. Ouyang and J. Ye, *ACS Catal.*, 2020, **10**, 4726–4736.

105 H. Wang, S. Fu, B. Shang, S. Jeon, Y. Zhong, N. J. Harmon, C. Choi, E. A. Stach and H. Wang, *Angew. Chem., Int. Ed.*, 2023, **62**, e202305251.

106 D. Liu, Y. Xu, M. Sun, Y. Huang, Y. Yu and B. Zhang, *J. Mater. Chem. A*, 2020, **8**, 1077–1083.

107 D. Mateo, N. Morlanes, P. Maity, G. Shterk, O. F. Mohammed and J. Gascon, *Adv. Funct. Mater.*, 2020, **31**, 2008244.

108 X. Liu, C. Xing, F. Yang, Z. Liu, Y. Wang, T. Dong, L. Zhao, H. Liu and W. Zhou, *Adv. Energy Mater.*, 2022, **12**, 2201009.

109 X. Zhu, H. Zong, C. J. V. Perez, H. Miao, W. Sun, Z. Yuan, S. Wang, G. Zeng, H. Xu, Z. Jiang and G. A. Ozin, *Angew. Chem., Int. Ed.*, 2023, **62**, e202218694.

110 Y. Li, J. Hao, H. Song, F. Zhang, X. Bai, X. Meng, H. Zhang, S. Wang, Y. Hu and J. Ye, *Nat. Commun.*, 2019, **10**, 2359.

111 A. Iglesias-Juez and J. M. Coronado, *Chem*, 2018, **4**, 1490–1491.

112 M. Behrens, F. Studt, I. Kasatkin, S. Kuhl, M. Havecker, F. Abild-Pedersen, S. Zander, F. Girgsdies, P. Kurr, B. L. Kniep, M. Tovar, R. W. Fischer, J. K. Norskov and R. Schlogl, *Science*, 2012, **336**, 893–897.

113 B. Xie, R. J. Wong, T. H. Tan, M. Higham, E. K. Gibson, D. Decarolis, J. Callison, K. F. Aguey-Zinsou, M. Bowker, C. R. A. Catlow, J. Scott and R. Amal, *Nat. Commun.*, 2020, **11**, 1615.

114 B. Xie, P. Kumar, T. H. Tan, A. A. Esmailpour, K.-F. Aguey-Zinsou, J. Scott and R. Amal, *ACS Catal.*, 2021, **11**, 5818–5828.

115 R. P. Ye, J. Ding, W. Gong, M. D. Argyle, Q. Zhong, Y. Wang, C. K. Russell, Z. Xu, A. G. Russell, Q. Li, M. Fan and Y. G. Yao, *Nat. Commun.*, 2019, **10**, 5698.

116 L. Zhang, G. Kong, Y. Meng, J. Tian, L. Zhang, S. Wan, J. Lin and Y. Wang, *ChemSusChem*, 2017, **10**, 4709–4714.

117 Z. Li, J. Liu, R. Shi, G. I. N. Waterhouse, X. D. Wen and T. Zhang, *Adv. Energy Mater.*, 2021, **11**, 2002783.

118 S. Ning, H. Ou, Y. Li, C. Lv, S. Wang, D. Wang and J. Ye, *Angew. Chem., Int. Ed.*, 2023, **135**, e202302253.

119 A. Caballero and P. J. Perez, *Chem. Soc. Rev.*, 2013, **42**, 8809–8820.

120 L. Luo, Z. Gong, Y. Xu, J. Ma, H. Liu, J. Xing and J. Tang, *J. Am. Chem. Soc.*, 2022, **144**, 740–750.

121 L. Luo, L. Fu, H. Liu, Y. Xu, J. Xing, C. R. Chang, D. Y. Yang and J. Tang, *Nat. Commun.*, 2022, **13**, 2930.

122 Y. Jiang, S. Li, S. Wang, Y. Zhang, C. Long, J. Xie, X. Fan, W. Zhao, P. Xu, Y. Fan, C. Cui and Z. Tang, *J. Am. Chem. Soc.*, 2023, **145**, 2698–2707.

123 L. Zhang, L. Liu, Z. Pan, R. Zhang, Z. Gao, G. Wang, K. Huang, X. Mu, F. Bai, Y. Wang, W. Zhang, Z. Cui and L. Li, *Nat. Energy*, 2022, **7**, 1042–1051.

124 L. Meng, Z. Chen, Z. Ma, S. He, Y. Hou, H.-H. Li, R. Yuan, X.-H. Huang, X. Wang, X. Wang and J. Long, *Energy Environ. Sci.*, 2018, **11**, 294–298.

125 H. Song, X. Meng, Z.-J. Wang, Z. Wang, H. Chen, Y. Weng, F. Ichihara, M. Oshikiri, T. Kako and J. Ye, *ACS Catal.*, 2018, **8**, 7556–7565.

126 B. Han, W. Wei, M. Li, K. Sun and Y. H. Hu, *Chem. Commun.*, 2019, **55**, 7816–7819.

127 J. Zhao, X. Guo, R. Shi, G. I. N. Waterhouse, X. Zhang, Q. Dai and T. Zhang, *Adv. Funct. Mater.*, 2022, **32**, 2204056.

128 Q. Hu, Y. Li, J. Wu, Y. Hu, H. Cao and Y. Yang, *Adv. Energy Mater.*, 2023, **13**, 2300071.

129 Z. Rao, Y. Cao, Z. Huang, Z. Yin, W. Wan, M. Ma, Y. Wu, J. Wang, G. Yang, Y. Cui, Z. Gong and Y. Zhou, *ACS Catal.*, 2021, **11**, 4730–4738.

130 L. Zhou, J. M. P. Martirez, J. Finzel, C. Zhang, D. F. Swearer, S. Tian, H. Robatjazi, M. Lou, L. Dong, L. Henderson, P. Christopher, E. A. Carter, P. Nordlander and N. J. Halas, *Nat. Energy*, 2020, **5**, 61–70.

131 D. Shen, Z. Li, J. Shan, G. Yu, X. Wang, Y. Zhang, C. Liu, S. Lyu, J. Li and L. Li, *Appl. Catal., B*, 2022, **318**, 121809.